SPECTRAL MEASUREMENTS OF IONIZATION AND DISSOCIATION IN INTENSE LASER PULSES

A Dissertation

by

YAKUP BORAN

Submitted to the Office of Graduate and Professional Studies of
Texas A&M University
in partial fulfillment of the requirements for the degree of

DOCTOR OF PHILOSOPHY

Chair of Committee,	Hans A. Schuessler
Co-Chair of Committee,	Alexandre A. Kolomenskii
Committee Members,	Olga Kocharovskaya
	Janet Bluemel
Head of Department,	Peter McIntyre

December 2017

Major Subject: Physics

ABSTRACT

Ionization and dissociation of molecules under ultrafast intense laser radiation could be used to study the structure of molecules and their dynamical response. Molecules or atoms are subjected to femtosecond laser pulses having different intensities and polarization orientations to be ionized or be dissociated. The work presented in this report can be separated into two main parts. The first part focuses on the interaction between femtosecond laser pulses and molecules, in particular, the dissociation of acetonitrile (CH_3CN). We study the production of positively charged fragment ions of acetonitrile (CH_3CN) in intense laser radiation having 800 nm wavelength, 50 fs pulse duration with a reflectron time-of-flight (TOF) ion mass spectrometer. The formation of positively charged fragments ejected from acetonitrile at different laser intensities, between 4.4×10^{13} W/cm^2 and 3.3×10^{14} W/cm^2, and with various polarization orientations was studied. Using the results on intensity dependent ion yields, appearance energies of fragments were determined and these results were compared with quantum chemical calculations, which were done with GAMESS. When the laser polarization direction was parallel or perpendicular to the TOF axis, the angular distributions of C^+ and C^{2+} ions showed maxima in both cases, while other fragments showed yield maxima, when the laser radiation was parallel to this axis. In addition, kinetic energy releases (KER) of H^+ ions ejected from acetonitrile were experimentally measured using the linear part of the TOF ion mass spectrometer. Angular distributions and intensity dependences of H^+ ions showed that three different photoionization mechanisms exist. Furthermore, KER of H^+,

H_2^+ and H_3^+ ejected from hydrocarbon molecule ethane (C_2H_6) were investigated experimentally by operating the TOFMS in the linear mode. Laser intensity and polarization dependences of these hydrogen ions were also studied in detail.

In the second section of this work, the interaction of laser radiation with sodium atoms is discussed. Photo-electron energy spectra for sodium atom is measured experimentally and it is found that electrons are mainly ejected from 5p, 6p and 7p states. Photo-electron angular distributions (PAD) from 5p state for zero, first, second and third order ATI is also determined. We observed that PADs of electrons depend on the number of photons absorbed by the electrons.

DEDICATION

To my brother, Yasin Boran.

To my wonderful wife, Zeynep Boran.

To my parents.

ACKNOWLEDGEMENTS

First of all I would like to thank my parents and my wonderful wife for providing me continuous support and encouragement throughout my years of study at Texas A&M University.

I would like to express my sincere gratitude and appreciation to my advisor, Hans A. Schuessler, for his guidance and for providing me a wonderful research opportunity in the atto laboratory. I especially would like to thank my co-advisor, Alexandre Kolomenski, for his help in the preparation of experiments, troubleshooting the equipment, interpretation of the experimental results and guiding me throughout the work on my dissertation. He is an excellent experimental physicist, who taught me many experimental technics and methods that improved my skills in the atto laboratory. I also would like to thank my committee members, Olga Kocharovskaya and Janet Bluemel for their guidance and support throughout this research. Especially, Dr. Bluemel provided us a variety of chemicals that were used in my research and gave me valuable advice. My thanks also go to James Strohaber, who has built the time-of-flight ion mass spectrometer in our atto laboratory. He also shared his knowledge about the time-of-flight ion mass spectrometer and brought new ideas to my research. In particular, he put forward the idea to measure the TOF of hydrogen ions in the linear time-of- fight mass spectrometer with his experimental apparatus. He also helped me to write MATLAB programs for analyzing data. His help was essential in completing my research project.

I am deeply grateful to Turkish Ministry of National Education, which has financially supported me during my education at Texas A&M University. My education would not have been possible without their support.

Finally, I would like to thank my friends, colleagues, faculty and staff of the Physics and Astronomy department for making my time here a great experience.

CONTRIBUTORS AND FUNDING SOURCES

This work was supported by a dissertation committee consisting of Prof. Dr. Hans A. Schuessler [advisor], Dr. Alexandre A. Kolomenski [co-advisor] and Prof. Dr. Olga Kocharovskaya of the Department of Physics and Astronomy and Prof. Dr. Janet Bluemel of the Department of Chemistry. All work on the dissertation was completed independently by the student, Yakup Boran.

This graduate study was supported by the Robert A. Welch Foundation, grant No. A1546 and the Qatar Foundation under the grant NPRP 6-465-1-091. Yakup Boran acknowledges support from the Ministry of National Education of the Republic of Turkey.

NOMENCLATURE

ATI	above-threshold ionization
ATD	above-threshold dissociation
CE	Coulomb Explosion
FAD	Field Assisted Dissociation
fs	femtosecond
HWP	Half Wave Plate
G	Grids
GAMESS	General Atomic and Molecular Electronic Structure System
KER	Kinetic Energy Release
LTOFMS	Linear Time-of-Flight Mass Spectrometer
MCP	Micro Channel Plate
MPI	Multiphoton Ionization
ps	picosecond
QET	Quasi-Equilibrium Theory
RTOFMS	Reflectron Time-of-Flight Mass Spectrometer
TI	Tunneling Ionization
TOF	Time-of Flight
TOFMS	Time-of-Flight Mass Spectrometer

TABLE OF CONTENTS

Page

LIST OF FIGURES

Page

LIST OF TABLES

Page

CHAPTER I

INTRODUCTION

1.1 Motivation

Light was crucial in the 19^{th} century physics. The combination of electric and magnetic fields into the electromagnetic field, that describes the light, was the most important success of this century. New investigations of the mysterious nature of light led to understanding its quantum mechanical properties, which belong to the main discoveries of twentieth century physics. Not surprisingly, in this 21^{st} century light-matter interactions continue to bring new findings. Over the past decades, understanding the interaction of atoms and molecules with intense laser light has become one of the most interesting and fertile research areas in atomic and molecular physics. Laser radiation is being used as a versatile and customizable research tool in variety of experiments. Since atomic and molecular motions occur on a time scale faster than a nanosecond, short laser pulses are needed to trace all the processes that can take place during the interaction of laser light with atoms and molecules. Recent developments in laser technology have allowed researchers to generate intense femtosecond (fs) pulses of light and very recently even sub-femtosecond and attosecond pulses of light have been obtained [1, 2]. To produce high density of power, the energy can be concentrated in time (short pulses), and the laser beam can be focused in a tiny area, which on the applied side can be of interest in applications to laser surgery and material cutting [3]. When fs pulses are focused to a few μm , peak intensities of the order 10^{12}-10^{15}W/cm^2 can be achieved. At such intensities the laser field becomes comparable to or even exceeds the Coulomb field which valence

electrons experience. At this high intensity regime many interesting phenomena related to the dynamics of atoms and molecules have been discovered. One or several electrons can be removed by absorption of several photons in the interaction with an intense laser field, which is called multi-photon ionization (MPI) [4, 5]. Sometimes these electrons can absorb an excess amount of photons during the ionization that leads to multiple peaks in the energy spectrum. This process was first observed by Agostini in 1979 [6], and later on it was named above-threshold ionization [7, 8]. In intense laser fields, there are two regimes for ionization processes, the tunneling regime and the multi-photon regime. These two regimes are distinguished based on the Keldysh parameter γ [9]. The Keldysh parameter depends on the laser frequency, the strength of the laser field and the ionization potential of the atomic or molecular system. Tunneling ionization takes place when the Keldysh parameter is less than one, and multi-photon ionization is dominant when Keldysh parameter is greater than one. A more detailed discussion on the Keldysh parameter will be given in the next section.

One type of instruments that has been widely used to study photo-dissociation and photo-ionization processes is a time-of-flight spectrometer. Such a device can detect ions, which is widely used in experiments. With this detection method the mass-to-charge ratio of fragments can be determined. Another option is measuring the ionized electron yields. Kinetic energies of the photo-electrons give more accurate information about the ionization processes. Luckily, our laboratory has both of these devices to measure ion and electron yields. Using these two instruments studies of many processes and phenomena, such as photo-dissociation dynamics of molecules [10, 11], field assisted dissociation

(FAD) [11, 12], Coulomb explosion (CE) [13, 14], and energy spectra and angular distributions of photoelectrons [15, 16] can be done. The above processes have been studied experimentally and theoretically by several research groups. For example, the dynamical behaviors of polyatomic molecules have been reported by Cornaggia and coworkers [17] and Strohaber et al [10]. Cornaggia identified double ionization of several polyatomic molecules such as N_2 and CO_2 from the ion yield measurements, using a strong linear polarized laser radiation. Strohaber studied ionization and dissociation of CH_4 using 50 fs pulses of laser light. In his work angular dependences and intensity dependences of ion yields have been measured. A fragmentation pattern with perpendicular to the polarization direction ejection was observed for CH_2^{2+}. Another interesting possibility is to measure the electron yields of alkali metals such as Li, Na and Cs. Since the alkali metals have their outermost electron in an s-orbital, they are easy to ionize. Schuricke et al [18] studied photo-electron energy spectra and angular distributions of Li at different laser intensities. They found that angular distributions change with increasing intensity. Selective excitation mechanisms of atomic Na were recently reported by Hart et al [8]. They observed that by varying the laser intensity, ac Stark shift of Rydberg states in Na and consequently ionization from different levels of electron can be controlled. In this way, a Freeman resonance [19], which resonantly enhances MPI can be realized.

When an atom or a molecule is exposed to intense laser radiation, a series of smaller fragment species can be formed or electrons can be removed from different energy levels. The interpretation of such mechanisms and analyzing the experimental data are complicated, and more experimental and theoretical study are needed for better

understanding of the relevant dissociation mechanisms. The work presented in this dissertation focuses mainly on studying the response of sodium atoms and acetonitrile molecules when they interact with short laser pulses. Ionization and appearance energies of acetonitrile have been determined experimentally and theoretically using the electron impact ionization method by several research group [20, 21]. Photo-dissociation and photo-ionization of acetonitrile in fs pulses was only reported for singly charged ions of CH_nCN^+ (n=0-3)[22]. In our work, we also provide information on other fragments by performing experiments on intensity dependences and angular distributions. This study is performed by using time-of–flight electron and mass spectrometers. Studying of laser-atom and laser-molecule interactions is important for understanding dynamics of atoms and molecules in strong laser fields. Different laser parameters such as intensity and polarization measurements are employed in experimental measurements, since these are powerful tools to study fundamental photoionization and dissociation processes.

1.2 Organization of the dissertation

This dissertation is grouped into eight chapters and organized as follows. In chapter 2, I will briefly review the interaction of atoms and molecules with intense and ultrashort laser pulses, which includes different ionization processes such as MPI, TI and ATI, as well as processes affecting dissociation such as bond softening and bond hardening. Chapter 3 will explain the experimental apparatus used in this research work. First, the laser systems used will be introduced. Then, the TOF electron and mass spectrometers will be discussed. The theory for linear and reflectron TOFMS will be provided. In chapter 4, experimental results on intensity dependences and angular distributions of acetonitrile under intense

laser radiation will be presented. In chapter 5, a detailed description and results are given on kinetic energy releases of protons ejected from the acetonitrile molecule. This was measured by the linear type TOFMS. Chapter 6 presents the experimental results on the photo dissociation of the hydrocarbon molecule C_2H_6. In addition, the hydrogen ion species (H^+, H_2^+ and H_3^+) were explored experimentally by again operating the TOFMS in the linear mode. In chapter 7, we move our focus to photoelectron spectra of Na. Here, experimental results of angular distributions of photoelectrons at different intensities is discussed. The last chapter gives overall conclusions and a general summary of the research performed in this dissertation.

CHAPTER II

LASER MATTER INTERACTIONS

2.1 The Keldysh adiabatic parameter and the ponderomotive potential

The ionization mechanism is usually determined by the so-called adiabaticity or Keldysh parameter γ that is related to the laser frequency and the tunneling frequency [23]:

$$\gamma = \frac{tunneling\ time}{laser\ period} \tag{2.1}$$

The Keldysh parameter is a useful to predict whether the ionization process will happen through tunneling ionization or multiphoton ionization, and it can be also defined in terms of the ponderomotive potential U_P and the ionization potential I_P,

$$\gamma = \sqrt{\frac{I_P}{2U_P}} \tag{2.2}$$

The ponderomotive energy is the average oscillation energy of a free electron in the radiation field, and it is a function of characteristic parameters of the laser light,

$$U_P = \frac{e^2 E_0^2}{4m\omega_0^2}, \tag{2.3}$$

where e is the electron charge, E_0 is the electric field strength, ω_0 is the angular frequency of laser field, and m is the mass of electron. The ponderomotive potential can be expressed in terms of intensity by using $I = c\epsilon_0 E_0^2 / 2$, and it turns into,

$$U_P = \frac{2e^2}{c\epsilon_0 m} \times \frac{I}{4\omega_0^2}\ , \tag{2.4}$$

where c is the speed of light, ϵ_0 is the dielectric constant in vacuum. Using atomic units, the ponderomotive energy can be written as

$$U_P[\text{eV}] = 9.33\times10^{-20}\times(\lambda[\text{nm}])^2\times I[\text{W/cm}^2]. \quad (2.5)$$

If $U_P > I_P$ strong field regime takes place for the ionization process. In 1965 Keldysh theoretically derived that multiphoton ionization and tunneling ionization are just two limiting regimes of nonlinear ionization. When the oscillation period is smaller than the tunneling time, $\gamma >> 1$, the ionization most probably will be through multiphoton ionization. If the laser oscillation period is greater than the tunneling time of the electron, $\gamma << 1$, then tunneling ionization is predominant. In Table 1 ponderomotive potentials and Keldysh parameters for acetonitrile, which has I_P=12.40 eV, are presented at different laser intensities.

Table 1 Ponderomotive potential and Keldysh parameter for CH_3CN at different laser intensities for 800nm wavelength.

Intensity (W/cm^2)	U_P (eV)	Keldysh parameter
5×10^{12}	0.299	4.56
1×10^{13}	0.598	3.22
5×10^{13}	2.988	1.44
1×10^{14}	5.976	1.02

The criteria for MPI and tunneling ionization can be summarized as following:

- MPI: high laser electric field and low ionization potential
- TI: Low laser electric field and high ionization potential

2.2 Multiphoton ionization

It is well known that the ejection of an electron from atoms or molecules by a photon can only take place when incident photon energy is greater than the binding energy of the electron. When the single photon energy is not high enough to overcome the atomic or molecular potential energy barrier, the energy of two or even more photons should be absorbed simultaneously to exceed the potential energy barrier. If the total energy of absorbed photons is larger than the ionization energy, an electron will be removed from the atom or molecule. This process is called multiphoton ionization (MPI), which takes place when an atom or molecule are subjected to intense laser radiation. At relatively low intensities, when n photons are absorbed, the electron reaches the energy state in the continuum and becomes a free electron. The ionization yield is the function of the intensity to the order equal to the number of absorbed photons, i.e $Y(\mathrm{I}) = I^n$, where n is the minimum number of photons required for the MPI process. When the electron is ejected after the ionization, the electron has the kinetic energy equal to $E_k = nh\omega - E_I$. Here, E_I is the ionization potential of the target atom or molecule.

2.3 Tunneling ionization

Under the laser irradiation with relatively low optical frequencies, such that $\gamma<1$, which is usually realized at intensities greater than $10^{14}\mathrm{W/cm}^2$, the Coulomb potential barrier

starts to be deformed and length of the barrier which electrons need to pass is decreased. Therefore, electrons might escape from atom or molecule through the barrier, and thus the system is ionized. This ionization process is referred to as tunneling ionization. Thus, if the electric field of the laser is so strong that it changes the atomic potential, quantum mechanical tunneling is more likely. In this process, the electron does not scatter on the system, but it is pulled to the edge of the system and can tunnel away from it. During the multiphoton ionization transitions between states having different energies occurs, but the transitions in tunneling ionization take place through a barrier, which means final and initial states have the same energy.

2.4 Above threshold ionization

Above threshold ionization (ATI) is an extension of multiphoton ionization process where an atom or molecule absorbs more photons than necessary to be ionized. An illustration of the ATI, MPI and TI processes is shown in Figure 1. The excess energy will be transferred to the electron, so that the more excess photons the higher the released electron will have kinetic energy. For each additional photon, a photoelectron peak in the energy spectrum appears. Consequently, a sequence of peaks separated by photon energy are observed in the ATI photo-electron energy spectrum. With the increasing intensity the peaks at higher energies appear. In order to determine the position of each ATI peak the following equation can be used,

$$E = (n+s)\hbar\omega - (I_P + U_P) \tag{2.6}$$

Where n and s represent the threshold number of photons required for ionization and the number of excess photon, respectively.

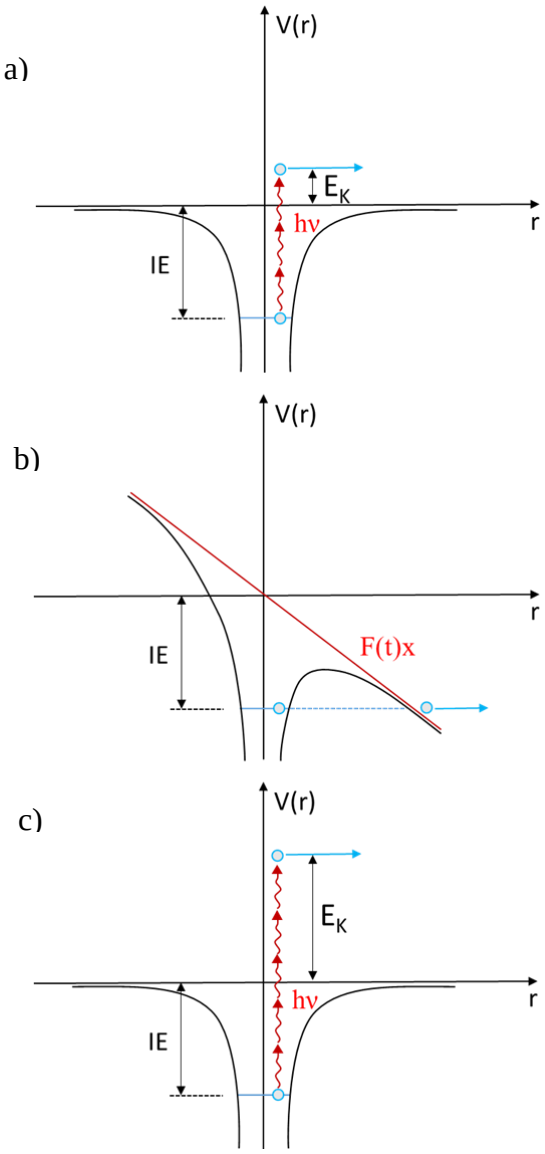

Figure 1. Ionization processes. Multi-photon ionization (a), tunneling ionization (b), and above threshold ionization (c).

The intensity of the laser field affects the number of peaks, intensity and width of the peaks in the electron spectra as well as angular distributions. On the other hand, electron kinetic energies in the spectrum are almost independent of the laser intensity because of the cancellation of the increased ionization potential of the target and the kinetic energy from the ponderomotive potential. If the pulse duration of the laser field is longer than the time for electron to leave the interaction region, the experiment is in a long pulse regime. In the short pulse regimes, ATI experiments show that peaks split up into a series of narrow peaks.

In long pulse experiments, ponderomotive potential is converted to kinetic energy and IP is raised, so that the effect of the ponderomotive potential itself can be clearly seen in the spectrum. For short pulse experiments, the time for a photo-ionized electron to leave the interaction region is longer than the laser field, so that electron does not have enough time to accelerate before the short pulse leaves. Thus, the energy spectrum shows the real photoelectron energies at the time of ionization.

2.5 Photo-dissociation

Photo-dissociation is the breaking of one or several bonds in a chemical compound through the absorption of photons. In this process, a gas target molecule interacts with one or more photons, and such an interaction can take place with visible as well with infrared light. Ultraviolet light, x-rays and gamma rays can also cause photo-dissociation, since the photon energy is sufficient to break the chemical bond of a molecule. The bonds in a molecule have different strength depending on the atoms in this molecule. For instance, N_2 molecule has triple bond while O_2 molecule has double bond. Consequently, breaking

the O_2 bond requires less energy than breaking the N_2 bond. The photo-dissociation process might occur with a single photon absorption or multiple photon absorption. When dissociation happens with single photon, which is mostly in UV region, the molecule is excited from the ground state to an excited state. In the case of multiphoton dissociation, commonly taking place in the infrared region, a molecule is promoted to an excited state via absorption of several photons. If the energy of the excited state exceeds the dissociation energy of the weakest bond, the molecule can be broken into fragments. In this study, our main focus is dissociation with multiple photons. A generalized photo-dissociation reaction can be defined as;

$$\begin{aligned} AB + nh\nu &\rightarrow AB^* \\ AB^* &\rightarrow A + B \end{aligned} \tag{2.7}$$

Here, the first step is absorption of n photons, which promote the molecule to the excited state, and the second step is photo-dissociation, which results in splitting the molecule.

2.6 Bond softening

Bond softening is defined as the reduction of bond strength in a molecule in the presence of strong laser light. This process was first observed by Bucksbaum et al. [24]. In order to observe this effect, the strength of the laser field needs to be comparable to the internuclear binding field. Such strong fields correspond to the laser intensities 10^{13}-10^{15} W/cm^2, and these intensities can be achieved using Ti:Sapphire lasers. In this process, the potential energy curve of a molecule is flattened (softened), so that the molecule dissociates. While dissociation via Coulomb explosion occurs by the sudden removal of electrons, the effect of the repulsion in bond softening is rather moderate, and no electron is removed from the

molecule. Molecular fragments resulting from bond softening have kinetic energies less than or equal to one photon energy.

2.7 Bond hardening

Bond hardening is the opposite effect compared to the bond softening, but both of them can be explained in the same theoretical terms [25]. Bond hardening is also called vibrational trapping or molecular stabilization. In bond hardening, the bond does not really become stronger, but the molecule enters a state having opposite properties to the bond softened state. The chance that the molecule will be photo-dissociated into smaller fragments decreases suddenly, especially for higher vibrational levels. The reason for this can be explained as follows: a portion of the initial vibrational population is trapped in the potential well formed by an avoided crossing. Since the potential energy curves are changed with the intensity of the laser field, bond hardening depends on the laser intensity. The potential well will not be deep enough to trap the population at low intensities and molecule dissociates via bond softening. On the other hand, if the intensity is too high, then the potential well will be distorted and the population will not be trapped which also results the molecule dissociates. In order to trap the molecule in the bond hardened state only narrow range of laser intensities can be used, which makes this process difficult to observe [25].

In Figure 2 (Frasinski at al. [25]), the bond hardening process is shown. At the intensity of 50 TW/cm^2, the ionization of the neutral molecule starts, and a wave packet is created by the absorption of photons. After a few fs the wave packet crosses the potential well while 3-photon gap is small. Because of the slope of the potential well, the wave

packet turns back and returns to the 3-photon gap. At this time, laser intensity is significantly higher, and the diabetic crossing through the 3-photon gap is less probable, so that the wave packet gets trapped in a bond hardened state.

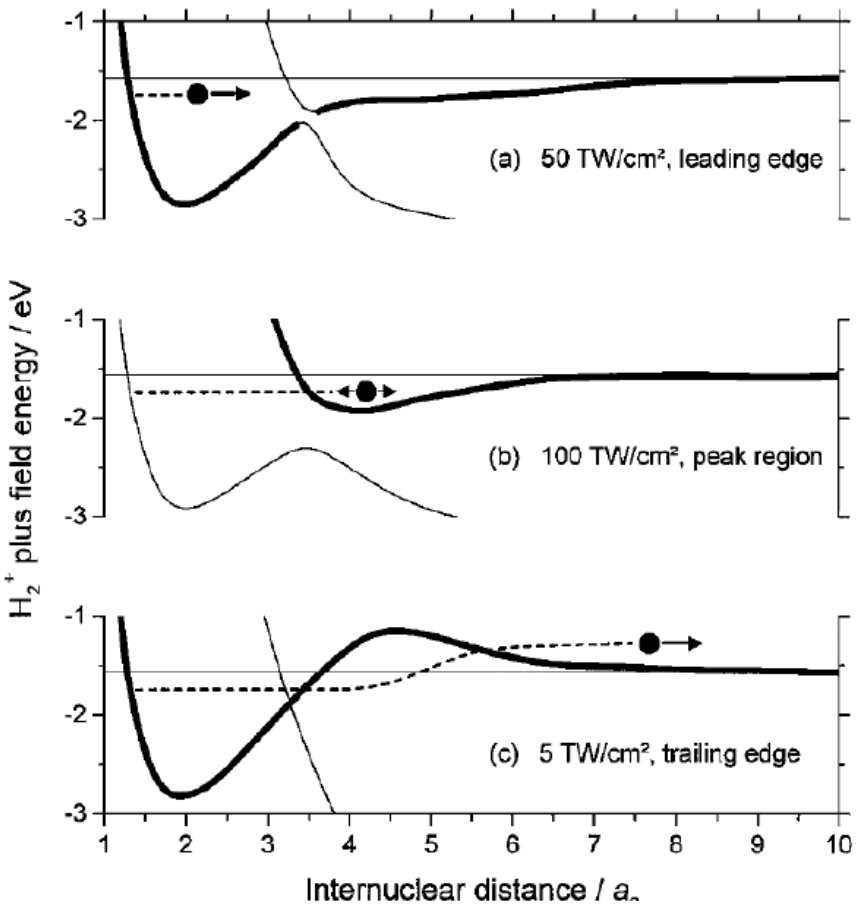

Figure 2. Bond hardening process for H_2^+. The H_2^+ ion is created on the leading edge of the laser pulse in the MPI process (a), the wave packet gets trapped in the bond hardened state (b), and the wave packet is lifted up and released with some kinetic energy. Reprinted from [25].

CHAPTER III

EXPERIMENTAL SETUP

In this chapter, first the high intensity laser sources used to ionize and dissociate the gas targets in a high vacuum will be described. Then the time-of-flight ion mass spectrometer, which measures the time-of-flight of positively charged ions, and the above threshold ionization (ATI) apparatus that measures the time-of flight of the electrons will be discussed.

3.1 Laser sources

In our laboratory, we use a Ti:Sapphire regenerative amplifier which delivers pulses of 1mJ in energy, 50 fs in duration at a repetition rate of 1kHz, and a wavelength close to 800nm. In order to achieve these high intense, ultrashort pulses several stages (see Figure 3) need to work together. The first stage is Verdi which is a solid-state, high power,

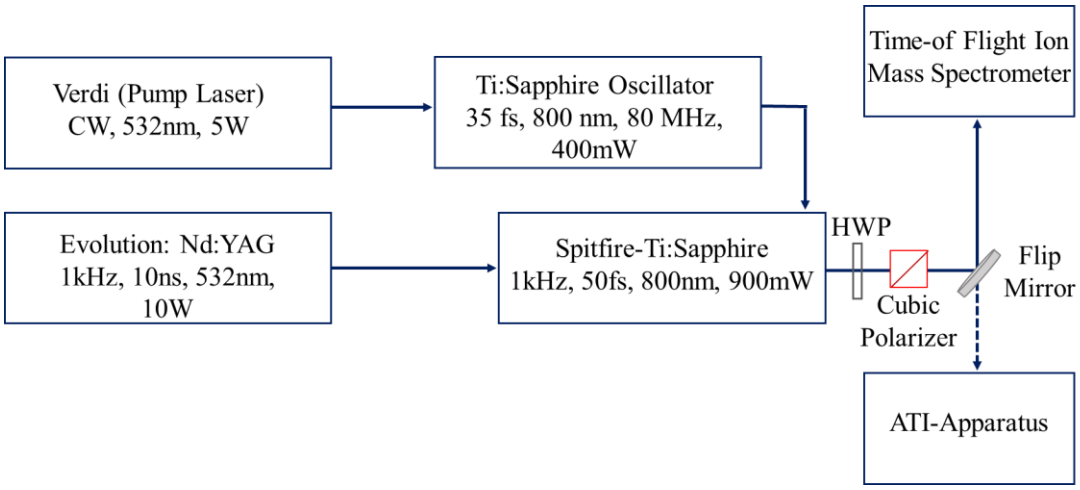

Figure 3. Layout and laser system.

continues wave (CW) laser. TheVerdi is used to pump the Ti:Saphire Kapteyn-Murnane (KM) oscillator and it supplies 5W of green 532 nm output, that is obtained by frequency doubling of 1064 nm laser pulse. When KM oscillator is pumped, theTi:Sapphire crystal produces random phase modes in the laser cavity. These random phases need to be locked together in order to generate pulse train. This mode-locking is achieved using the optical Kerr effect. The KM oscillator produces weak 5nJ, 35fs and 800nm pulses at a repetition rate of 80 MHz. The next stage for generating ultrashort pulses is chirped pulsed amplification (CPA) [26]. Seed pulses from oscillator are amplified in the Spectra Physics TSA Spitfire regenerative laser amplifier. This amplification is achieved by CPA technique. In this technique, the stretcher temporally expand the seed pulses to much longer durations to not exceed the damage threshold of the Ti:Sapphire crystal during the

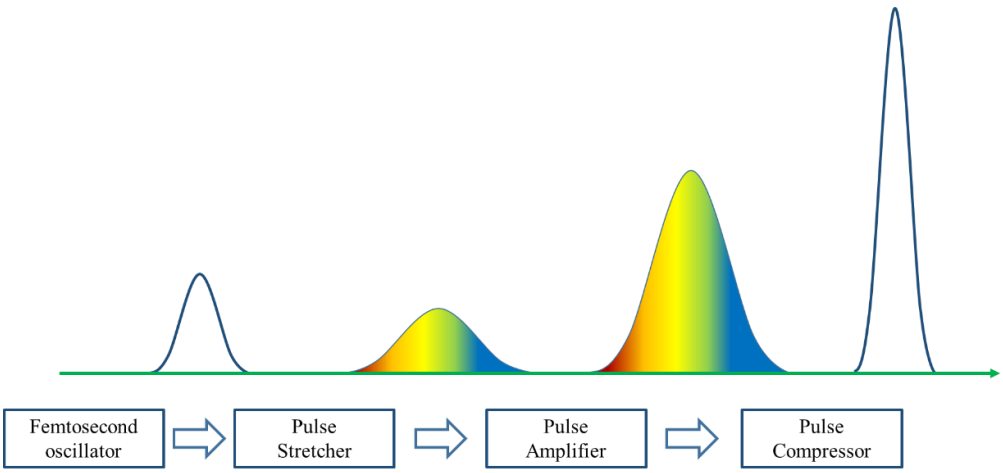

Figure 4. Diagram for the laser system using the CPA technique.

amplification. Then stretched pulses are amplified through stimulated emission in regenerative cavity. At the last stage, a grating compressor shortens the amplified pulses in the time domain. A schematic for CPA technique is shown in Figure 4. At the end, the Spitfire produces pulses having 50 fs duration, 800nm wavelength at a repetition rate of 1 kHz and an average power of ~900 mW.

3.2 Time-of-flight mass spectrometer

Time of flight mass spectrometer (TOFMS) has been an invaluable instrument across a wide range of applications since the time of flight resolution had been improved significantly during the last two decades. TOFMS has been widely used as an experimental apparatus in the study of interactions of atoms and molecules with intense and ultrashort laser radiation. The interaction of laser pulse and molecules in the focal region results ionization and dissociation of these molecules. Time-of-flight mass spectrometry is a method of mass spectrometry in which ions having different masses can be separated by using their time-of-flights. The time for an ion to travel over a known distance, from ionization region to a detector, is measured. TOF is depend on the mass and charge of the ion. Knowledge of TOFs can be used to determine molecular or atomic masses of chemical species. Materials need to be at the gas phase to be analyzed, but solid and liquid materials can also be used after they are evaporated by heating or using some other methods. In our experiments, linear and reflectron type TOFMS are used. Both devices are on the same vacuum chamber and rearranging the voltages on the grids switches them from one mode to the other. In next section, these two mass spectrometers will be explained in details.

3.2.1 Linear time-of-flight mass spectrometer (LTOFMS)

LTOFMS is a most commonly used spectrometers. They are simple to design but mass resolution is smaller than other spectrometers such as reflectron-TOFMS. The ions originated in the ionization region move in only one direction to the detector. A schematic of combined linear and reflectron type TOFMSs are shown in Figure 5. Laser radiation is focused into the ionization chamber between a repeller plate and a slit plate. An electric field is applied to accelerate the ions originated in the focal region of laser field so that their TOFs can be measured while they drift in a field free region which is called flight tube. Using a difference of potential applied between the repeller plate and the slit plate, ions are accelerated into the flight tube. When an accelerating field is applied to the ions, their kinetic energies will be identical, but ions having different mass to charge ratio will have different velocities, so that their arrival time will be different. Ions with lower masses have higher velocities and ions with higher masses have lower velocities. Using the

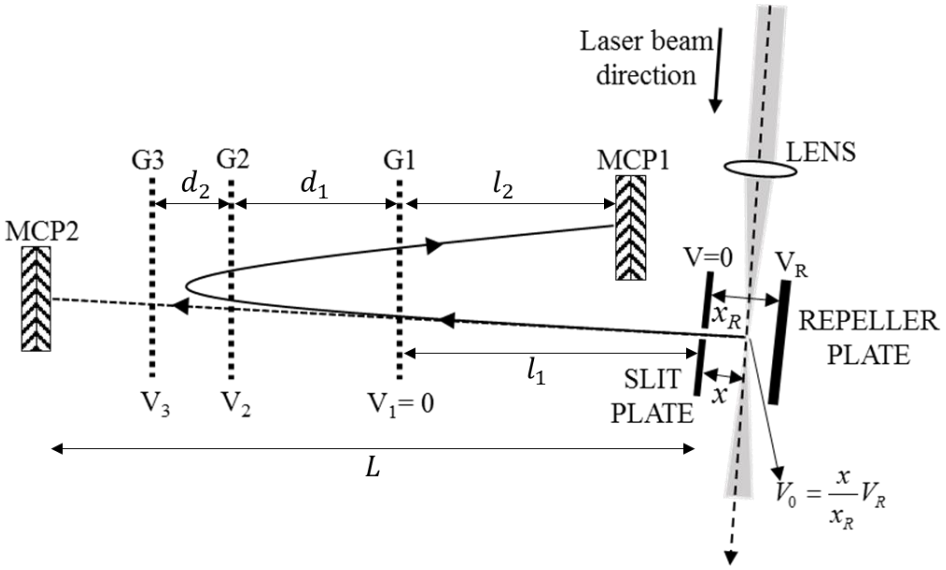

Figure 5. Schematic of the reflectron type time-of-flight mass spectrometer showing the reflected and direct paths. The dotted lines represent grids (G) held at fixed potentials. The microchannel plate for linear mode is MCP2 and that of reflected mode is MCP1.

acceleration voltage and distance of the detector from the ionization region, one can calculate the m/q ratios by measuring the flight time.

Since sub-relativistic velocities are used in TOFMS, the theory is simply described using Newtonian physics. The electric potential difference in a uniform electric field is given by

$$\Delta V = Ed \tag{3.1}$$

A force F acting on a charge q by the electric field E is given by

$$F = qE \tag{3.2}$$

A charged particle which is free to move in a uniform electric field behaves in a similar way to a particle in a gravitational field. One can find the acceleration in the TOF region by modifying the Newton's second law:

$$a = \frac{F}{m} = \frac{Eq}{m} \tag{3.3}$$

Potential energy of a charged particle in a uniform electric field is:

$$E_P = qV \tag{3.4}$$

When a charged particle is accelerated into TOF field free tube by the potential difference V, the potential energy will be converted into kinetic energy. Using this kinetic energy, velocity of the particle can be calculated as following:

$$E_k = \frac{1}{2}mv^2 = qV \tag{3.5}$$

After solving the above equality for v, velocity of the particle is found to be:

$$v = \sqrt{\frac{2qV}{m}} \tag{3.6}$$

Here potential $V = V_R \frac{x}{x_R}$, where V_R is potential on repeller plate, x_R is the distance between slit plate and repeller plate, x is the distance between slit plate and interaction region. Then Eq. (3.6) turns into:

$$v = \sqrt{\frac{2qxV_R}{mx_R}} \tag{3.7}$$

In the following equations, TOFs of a particle will be calculated for each region.

Region 1 (from ionization region to slit plate

The time ion will spend from ionization region to slit plate is

$$t_1 = \frac{v_s}{a_1} \tag{3.8}$$

where v_s is the velocity of particle at slit plate and a_1 is the acceleration of particle in region 1. a_1 can be found using the Eq. (3.3) and (3.5);

$$a_1 = \frac{qE}{m} = q\frac{V_R}{mx_R} \tag{3.9}$$

v_s is given by Eq. (3.7). Then t_1 can be found by

$$t_1 = \sqrt{\frac{2xx_R}{V_R}}\sqrt{\frac{m}{q}} \tag{3.10}$$

Region 2 (From slit plate to MCP)

In this region there is no acceleration field so that ions will fly freely without changing the velocity. High vacuum is necessary to allow ions fly freely without undergoing any collision with other species. Such collisions might cause unwanted reactions so that the mass spectrum will be more complex. The time an ion will spend in this free region simply can be calculated by:

$$t_2 = \frac{L}{v_s} \tag{3.11}$$

where L is the distance between slit plate and MCP. After plugging the Eq. (3.7) into Eq. (3.11), the TOF between slit and MCP will be:

$$t_2 = L\sqrt{\frac{m}{q}}\sqrt{\frac{x_R}{2xV_R}} \tag{3.12}$$

The total flight time for the linear mode of operation is the summation of t_1 and t_2;

$$t_{lin} = L\sqrt{\frac{m}{q}}\sqrt{\frac{x_R}{2xV_R}} + \sqrt{\frac{2xx_R}{V_R}}\sqrt{\frac{m}{q}} \tag{3.13}$$

Equation (3.13) can be written in a simpler form that gives the formula for the linear time of flight;

$$t_{lin} = \sqrt{\frac{m}{q}}\sqrt{\frac{x_R}{V_R}}\left(\frac{L+2x}{\sqrt{2x}}\right) \tag{3.14}$$

3.2.2 Reflectron type time-of-flight mass spectrometer

The mass resolution can be improved using an electrostatic reflector, also referred to as a reflectron. In 1973, a new type of mass spectrometer that is called reflectron time-of-flight mass spectrometer (R-TOFMS) was developed by B. A. Mamyrin [27]. R-TOFMS have a number of advantages over linear TOFMS. Since ions' direction of motion will be reversed in R-TOFMS, the total flight path of ions will increase hence the mass resolution will be increased. The reflectron also provides temporal focusing which helps to lower the time –of –flight distribution at the detector. As a result of reducing the time-of-flight distribution and having larger flight time will extremely enhance the mass resolution. Reflectrons create a deceleration field which acts as an ion mirror by deflecting and sending the ions back.

The reflectron that is consisted of three grids redirect the incoming ions at the end of the field free flight path using a suitable electrostatic field. Lower energetic ions penetrate less deep into reflectron grids than higher energetic ions. Subsequently, faster ions spend more time in the reflectron grids than slower ions. As a result, ions with different kinetic energies but the same mass to charge ratio will arrive at the MCP simultaneously which results in improved time focusing.

The equations for RTOFMS are obtained with similar way to LTOFMS, but here reflectrons need to be considered so that equations will be different. The motion of ion is the same until they arrive at the first grid which is held at ground potential. If the distance between slit plate and first grid is l , then the time ion will spend from ionization region to slit plate is;

$$t_{lin} = \sqrt{\frac{m}{q}}\sqrt{\frac{x_R}{V_R}}\left(\frac{l+2x}{\sqrt{2x}}\right) \tag{3.15}$$

Region 3 (Time between first and second grid)

At the end of the field free path ion will penetrate into reflectron grids where deceleration is present. Here, first grid is held at ground potential V_1, second grid is held at V_2 and the distance between first and second grid is d_1 . When ions enter this region, it will decelerate. If ion has enough kinetic energy, it will pass through second grid. Otherwise, it will turn around between first grid and second grid. TOF between first grid and second grid can be calculated as following:

$$t_3 = \frac{2}{a_3}(v_1 - v_2) \tag{3.16}$$

Since ion will spend the same time while penetrating into and reflecting from grids, multiplication of 2 is needed to find the TOF. Here v_1 and v_2 are velocities at first and second grids. Acceleration of an ion in this region is given by

$$a_3 = \frac{qV_2}{md_1} \tag{3.17}$$

v_1 is already defined in Eq. (3.7). Similarly v_2 can be written as;

$$v_2 = \sqrt{\frac{2qxV_R}{mx_R} - \frac{2qV_2}{m}} \tag{3.18}$$

If v_1 , v_2 and a_3 are inserted into Eq.(3.16), it will give the TOF in region 3,

$$t_3 = \frac{2d_1}{V_2}\sqrt{\frac{m}{q}}\sqrt{\frac{V_R}{x_R}}\left(\sqrt{2x} - \sqrt{2x - \frac{2x_R}{V_R}V_2}\right) \tag{3.19}$$

Region 4 (Time between second and third grid)

Similar formulas can be also used here as following:

$$t_4 = \frac{2}{a_4}(v_2 - v_3) \tag{3.20}$$

$$a_4 = \frac{q(V_3 - V_2)}{md_2} \tag{3.21}$$

$$v_3 = \sqrt{\frac{2qxV_R}{mx_R} - \frac{2qV_3}{m}} \tag{3.22}$$

$$t_4 = \frac{2d_2}{(V_3 - V_2)}\sqrt{\frac{m}{q}}\sqrt{\frac{V_R}{x_R}}\left(\sqrt{2x - \frac{2x_R}{V_R}V_2} - \sqrt{2x - \frac{2x_R}{V_R}V_3}\right) \tag{3.23}$$

Total TOF t_{total} will be summation of, t_{lin}, t_3 and t_4 .

$$t_{total} = t_{lin} + t_3 + t_4 \tag{3.24}$$

The TOF equations derived for reflectron time-of-flight ion mass spectrometer can be also found in [23].

3.2.3 Theoretical and experimental dispersion curves

Before using reflectron type TOFMS one needs to make sure that ions fly toward the MCP. To success this, parameters such as focal position and potentials on the repeller plate and reflectrons must be adjusted precisely. Dispersion curves helpful to get an idea where the focal position should be between repeller plate and slit plate and what voltages should be

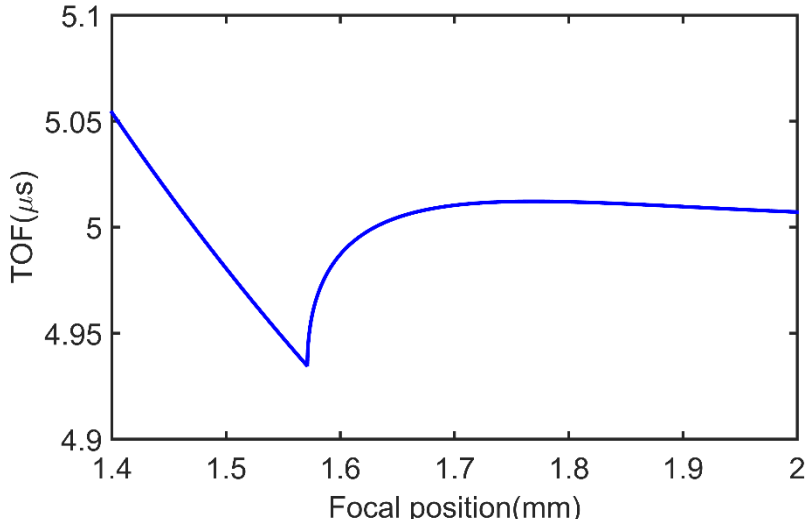

Figure 6. Dispersion curve for H^+ obtained using TOF equation.

used on repeller plate and reflectrons. Using the TOF equation one can get the dispersion curve easily for the desired parameters. In Figure 6 the dispersion curve for H^+ is simulated for the parameters V_R=1530V, V_1=802V and V_2=1052 using MATLAB. For comparison dispersion curve for H^+ is obtained experimentally using the same parameters used in simulation. To get the dispersion curve, H^+ ions fragmented from acetonitrile are used. Focal position is moved between slit plate and repeller plate using the translation stage. The distance between 1.4mm and 2mm is scanned with 60 different positions. For each position, TOF of H^+ is measured. This experiment is repeated using two different intensities $1.5x10^{14}W/cm^2$ and $3x10^{14}W/cm^2$. The result of these measurements are shown in the Figure 7.

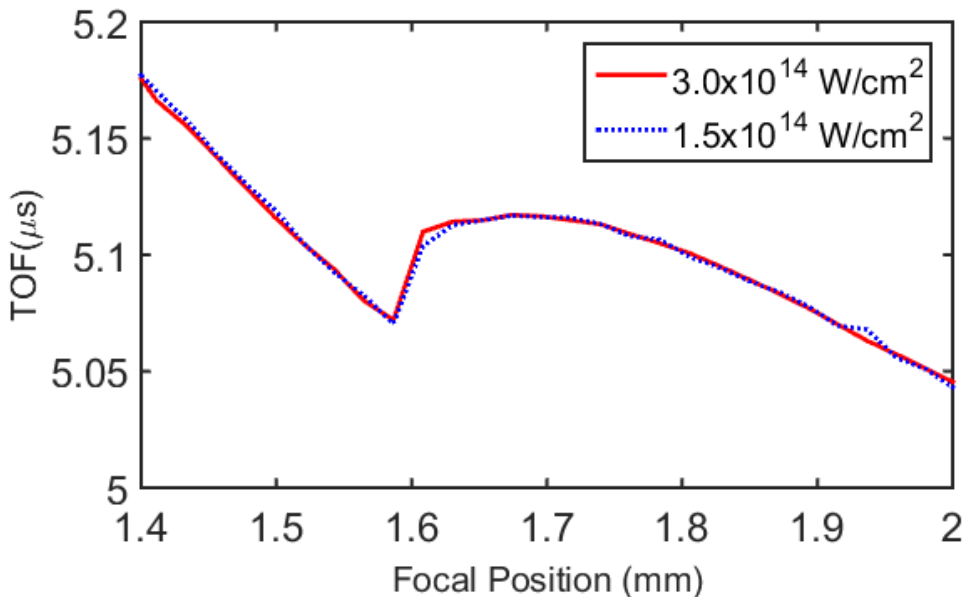

Figure 7. Experimental dispersion curves for H^+ for two different intensities.

3.2.4 Calibration of mass spectrum

In order to convert measured flight times into mass to charge ratio a calibration is performed. The reason for performing calibration is because of the time delay which is the result of mismatch between triggering of the counting card and the time when laser pulse is at the ionization region. This delay also can be because of electronic delay (for instance cables affect the arrival times). One needs to find delay time to get mass to charge ratio with great accuracy. One way to find the delay time is that TOFs of well-known ions are recorded and then this values can be plotted as a function of $\sqrt{M}$. After fitting these points to a straight line, delay time d_t and theoretical TOF of H^+ t_H can be determined. t_d is the value of y-intercept and slope of this straight line gives the t_H . Theoretical TOF of an ion having mass M and charge Q is given by

$$t_{theory} = \sqrt{\frac{M}{Q}} t_H \tag{3.25}$$

Where t_H is theoretical TOF of hydrogen ion (in this case M and Q are equal to 1). Theoretical TOFs are greater than experimental TOFs by a delay time $t_{\exp} = t_{theory} - t_d$. If this equation is plugged in Eq.(3.25) , the experimental TOF of an ion having mass M and charge Q will be

$$t_{\exp} = \sqrt{\frac{M}{Q}} t_H - t_d \tag{3.26}$$

When Eq. (3.26) is solved for M / Q,

$$\frac{M}{Q} = \left(\frac{t_{\exp} + t_d}{t_H} \right)^2 \tag{3.27}$$

An example of mass spectrum calibration is shown in Figure 8. Time of flight of H^+, H_2O^+, N_2^+ and O_2^+ are plotted as a function of $\sqrt{M}$. t_d and t_H are found to be -0.65 and 5.09 µs. Now using the t_d and t_H values experimental TOFs of all other ions can be determined precisely.

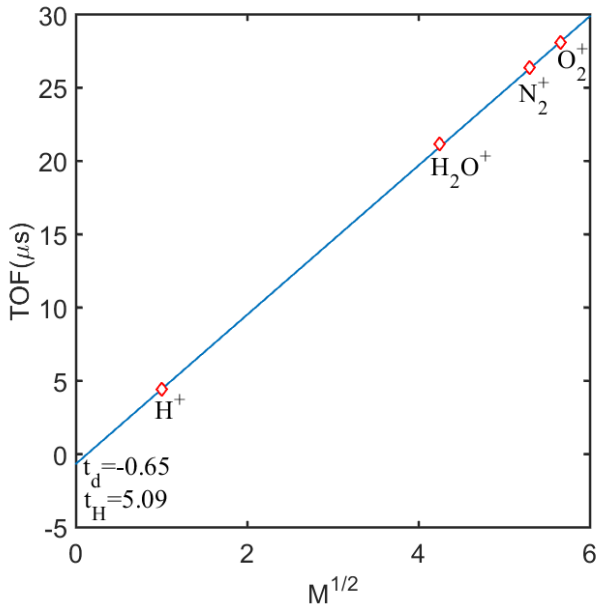

Figure 8. TOF vs $M^{1/2}$ to find the timing delay for calibration of the mass spectrum.

3.2.5 Data acquisition system

Fast processing of the signal obtained from MCP, which is accomplished by using fast digitization of the analog signal is an important part of the TOF-MS. The model MCS6 multiple event time digitizer converter (TDC) from FastComTec, having 100ps time

resolution was used in our experiments. Trigger signal is connected to the START channel and the signal from the detector is connected to one of the STOP channels. The output

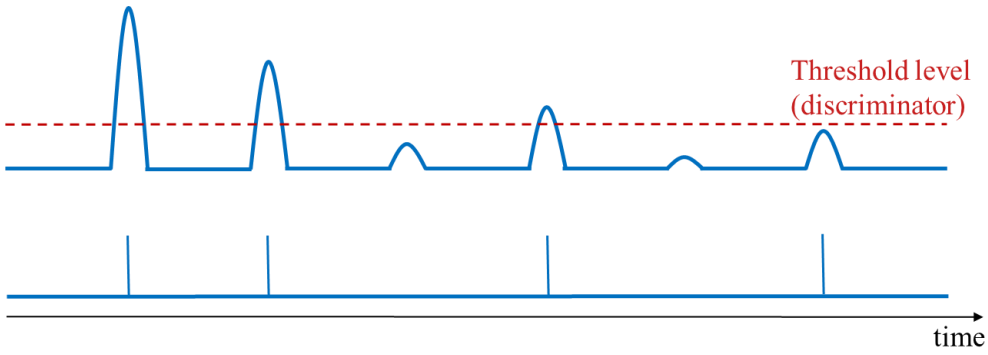

Figure 9. Simple illustration of the time to digital converter (TDC). Threshold level (discriminator) is presented in the top panel with dashed red line. The lower panel shows the signals that are counted by TDC.

signal from the TDC is transferred to the computer with a high speed USB ports. The arrival times of ions are recorded by TDC in binary format. Threshold level is used to select minimum pulse amplitudes being counted (see Figure 9). The TDC will not count any pulses with amplitudes, which are below the selected threshold level.

3.2.6 Detection system (Multichannel plate)

In our experiments, microchannel plates (MCP) detectors from Del Mar Photonics are used to detect the ions. A microchannel plate has tiny tubes (microchannels) distributed over its surface. These channels work as independent electron multipliers, and they are tilted at an angle of 5 to 15 degrees, so that an electron entering the channel hits the surface

of the channel. As a result, secondary electrons will be emitted after this initial collision. These secondary electrons are accelerated by an electric field set by a voltage applied to MCP. Those secondary ions also strike the surface of the channel, and more secondary electrons are produced. During this process, depending on the voltage and property of the MCP, the number of electrons will be multiplied by several orders of magnitudes.

A mini circuit ZKL-2 pre-amplifier having 10-2000MHz frequency bandwidth and 33.5 Db gain is mounted between the MCP and the data acquisition card to amplify the signal measured with the MCP detector.

3.2.7 Vacuum system and pressure measurements

TOFMS has an ultra-high vacuum pumping system with two turbo molecular pumps, which are connected to the ionization chamber and time of flight tube, and one roughing pump. The roughing pump (Scrollvac SC 15D) is connected to the exhaust of the turbo molecular pump to produce a pressure low enough (usually around 10^{-3} mbar) for the turbo molecular pump to work efficiently. Turbo pumps are from Oerlikon Leybold Vacuum and controlled by a Leybold Heraeus Turbotronic NT 151/361 controller. In experiments the pressures in two main chambers are measured with two ion gauges. Both of them are Oerlikon Leybold Vacuum ITR 90 and they are capable to read pressures in the range of 1000mbar to 5×10^{-10} mbar . Oerlekon Leybold Vacuum Three Center controller is used for both ion gauges.

3.3. ATI apparatus

Above threshold ionization apparatus is a TOF spectrometer which measures the TOF of electrons ejected from atoms or molecule. Figure 10 represents the schematic of ATI apparatus. ATI apparatus consists of a vacuum chamber, turbo molecular pump (Pfeifer Vavuum) and an ion gauge (Oerlikon Leybold Vacuum ITR 90) to monitor the pressure

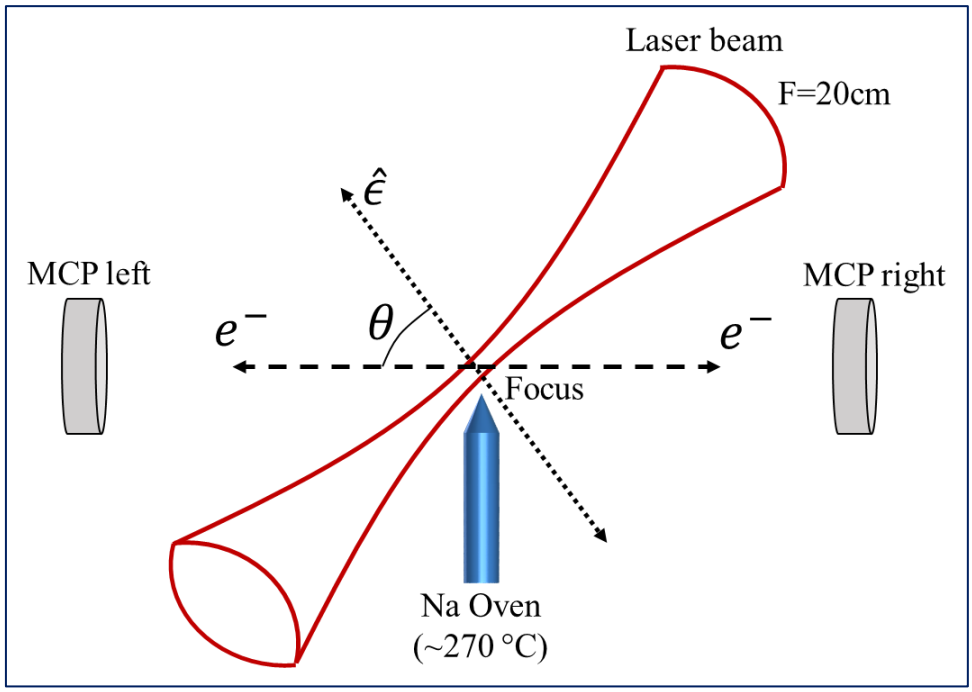

Figure 10. Schematic of the ATI apparatus. ∈ is the polarization of the laser beam. θ is the angle between polarization direction and detection axis.

inside the vacuum chamber. The vacuum chamber can be filled with any of the gas to the desired pressure using an adjustable leak valve. In our experiments with Na atoms, which form a solid at room temperature, the leak valve was not used. Instead, to evaporate Na

atoms an oven was used, which was installed inside the chamber. Linearly polarized laser radiation was focused into the center of the ATI chamber by using a 20 cm achromatic lens. About 1.5 cm below the focal point, the oven with sodium was located. Using the translation stage, Na beam was moved to the laser focal point, and the maximum integrated photoelectron yield from the ATI apparatus was achieved. The temperature of the oven was kept around 270 °C that created a pressure Na vapor of 1×10^{-7} mbar. The ejected electrons travel inside the field-free μ-metal and then are detected at the MCPs, located at the right and left ends of the flight tube. The same amplifier (ZKL-2 Mini Circuit), and the data acquisition system as in the TOF experiments with ions were also used to measure the photoelectron yields.

CHAPTER IV

DISSOCIATIVE IONIZATION OF ACETONITRILE IN INTENSE LASER FIELDS[1]

In this chapter, experimental results of the interaction between femtosecond laser pulses and acetonitrile (CH_3CN) molecules using a reflectron time-of-flight (TOF) ion mass spectrometer will be discussed. Ionization and dissociation of molecules in ultrafast and intense laser fields can be used to study the structure of molecules and their dynamical response. Molecules or atoms are subjected to femtosecond laser pulses having different intensities and polarization orientations to be ionized or be dissociated. Using the results on intensity dependent ion yields, appearance energies of fragments can be determined. Angular distributions give important information about dissociation dynamics of the molecules.

4.1 Introduction

The interaction of intense laser fields with atoms and molecules leads to strong field phenomena such as multiphoton ionization (MPI), tunneling ionization (TI), and Coulomb explosion (CE) [4, 13, 17, 28-31]. By focusing amplified femtosecond laser radiation peak intensities of $10^{15}\,W/cm^2$ are routinely achieved. Strong laser fields affect properties and structure of molecular systems that are different than those found for atomic systems. In previous experiments, the ionization and dissociation of small molecules such as CH_4,

[1] Part of this chapter is reprinted with permission from "Dissociative ionization of acetonitrile in intense femtosecond laser fields." by Y. Boran, A. A. Kolomenskii, M. Sayrac, N. Kaya, H.A. Schuessler and J. Strohaber. J. Phys. B: At. Mol. Opt. Phys. 50 (2017) 135003. doi.org/10.1088/1361-6455/aa6f52,

C_2H_6, CO_2, NO_2, H_2, and N_2 have been studied [3, 5, 10, 32-34], and various processes such as asymmetric fragmentation were observed. A removal of one or several electrons from a molecule by the laser field can result in a photo-dissociation process. At low peak intensities, singly-charged ions may be observed, and the yields are described by MPI, where the power law dependence $Y \propto I^n$ can be used to determine the number of photons required to ionize the molecules. Above an intensity, where a significant portion of molecules is ionized, the ionization mechanism tends to scale as $Y \propto I^{3/2}$ due to the volume averaging effect [10]. Currently, the understanding of the dissociation of polyatomic molecules in intense laser field is an ongoing challenge, and more experimental and theoretical studies are required to understand relevant dissociation mechanisms.

In this study, we report on experimental results for the ionization and photo-fragmentation of acetonitrile using a reflectron time-of-flight ion mass spectrometer. Acetonitrile, also known as methyl cyanide, is of interest to researchers, since it is the simplest organic nitrile compound [35, 36]. Acetonitrile and its fragments are essential in the study of the origins of life. It has astrophysical importance [37] and was found in comets, in interstellar clouds and in the Earth's stratosphere [38]. For these reasons, it is important to understand the strong field fragmentation of acetonitrile. Ionization and dissociation of acetonitrile has previously been studied experimentally and theoretically by several groups using electron impact and photoelectron techniques [20, 39-41]. However, data on the dissociative ionization of acetonitrile in femtosecond fields are scarce. From electron impact ionization experiments, the dissociation of acetonitrile, and appearance energies have been determined from energy distribution [39]. Photoionization

and photo-dissociation of acetonitrile was reported for experiments in the intensity range of 6.3×10^{13} to $1.2\times10^{14}\,W/cm^2$ with 50fs, 800-nm pulses of radiation [22]. In this previous work, detection of the singly charged fragment ions CH_nCN^+ (n=0-3) and the mechanism of photo-dissociation was reported, but no information on other fragments was provided. We performed a detailed study of all photo-fragments of acetonitrile and measured the angular and intensity dependences of the observed fragments. Our work is supplemented by quantum chemical calculations for the ionization and appearance energies using GAMESS (General Atomic and Molecular Electronic Structure System), and the results are compared with those from our experiments.

4.2 Experimental details

Our experimental setup consisted of a mode-locked, 800-nm Ti:sapphire laser system delivering 50 fs, 1 mJ pulses at a repetition rate of 1kHz. For intensity scans, a half-wave plate and a polarization cube were placed into the path of the laser beam. When rotating the polarization for angular scans, the polarization cube was removed, and the wave-plate was positioned directly in front of the entrance window. Figure 5 depicts the time-of-flight apparatus for operation with reflected and direct ion paths. The ionization chamber and the flight tube of the spectrometer were evacuated to a pressure of $\sim9\times10^{-9}$ mbar. Acetonitrile (99.9% purity) was vacuum distilled in a separate chamber and then introduced into the ionization chamber through a leak valve to an operating pressure of 5×10^{-7} mbar. Laser radiation was focused into the ionization chamber between a slit and a repeller plate by a lens having a focal length of 22.7 cm. The size of the slit was 400 μm

by 12 μm, and the slit was separated from the repeller plate by a distance of 3mm. The repeller plate had a positive voltage of 1.5 keV, while the slit plate was held at ground potential. Ions created in the focal region were accelerated toward the slit by the electrostatic field created between the plates. Because the laser beam has a spatial extent, ions having the same mass-to-charge ratio and originating at different positions will enter the flight tube with different kinetic energies. For this reason, these ions will have different flight times. To solve this problem, the TOF spectrometer was constructed with a set of grids (ion mirrors) to reflect ions back onto a detector (MCP1). Ions with larger kinetic energies penetrate deeper into the reflecting grids, while ions with smaller kinetic energies penetrate less deep so that, with suitably adjusted voltages on the grids, all ions arrive at the detector at the same time. Figure 11 shows calculated TOF dispersion curves of the parent CH_3CN^+ and the deprotonated ions CH_2CN^+ with respect to their initial positions in the ionization region. The flat part of the curves (around 1.7mm-2.0mm) demonstrates that ions having the same mass-to-charge ratio and originating within this region in the focal spot arrive at the detector at nearly the same time. The TOF separation of these ions having masses of 41amu and 40amu is shown in Figure 11 to be about 400ns. For lighter fragments, the TOF separation is larger i.e., the time separation between C^+ and CH_2^+ is around 1400ns. To detect ions, microchannel plate (MCP) detectors were used, and a broadband preamplifier (Mini Circuits ZKL-2, 500MHz frequency bandwidth) was employed to amplify the ion signal from the MCPs. The signals were then recorded using a multiscalar (MCS6, FAST ComTec) having a 100ps time resolution.

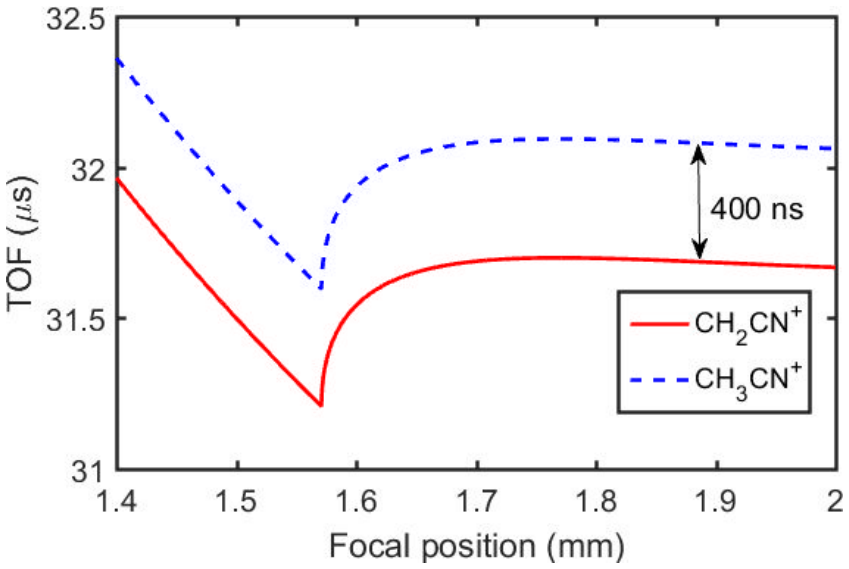

Figure 11. TOF for CH_3CN^+ (dashed blue) and CH_2CN^+ (solid red) ions. The time separation between these ions of about 400ns is shown. The focal position shows the distance from the slit plate.

4.3 Mass spectrum of the CH_3CN

The time-of-flight mass spectrum of acetonitrile irradiated by laser pulses with a peak intensity of $3\times10^{14}W/cm^2$ is shown in Figure 12. The mass spectra were measured using linear polarization (horizontal, along the TOF axis; and vertical, perpendicular to the TOF axis). The CH_2CN^+ ion peak at m/q = 40 was the dominant peak for the different polarization orientations. The ions of CH_nCN^+ (n=0-3) show similar shapes in the mass spectra for both vertical and horizontal polarizations. The peaks with mass to charge ratio *m/q* = 18, 28, and 32 are from H_2O^+, N_2^+, and O_2^+, and originate from residual atmospheric

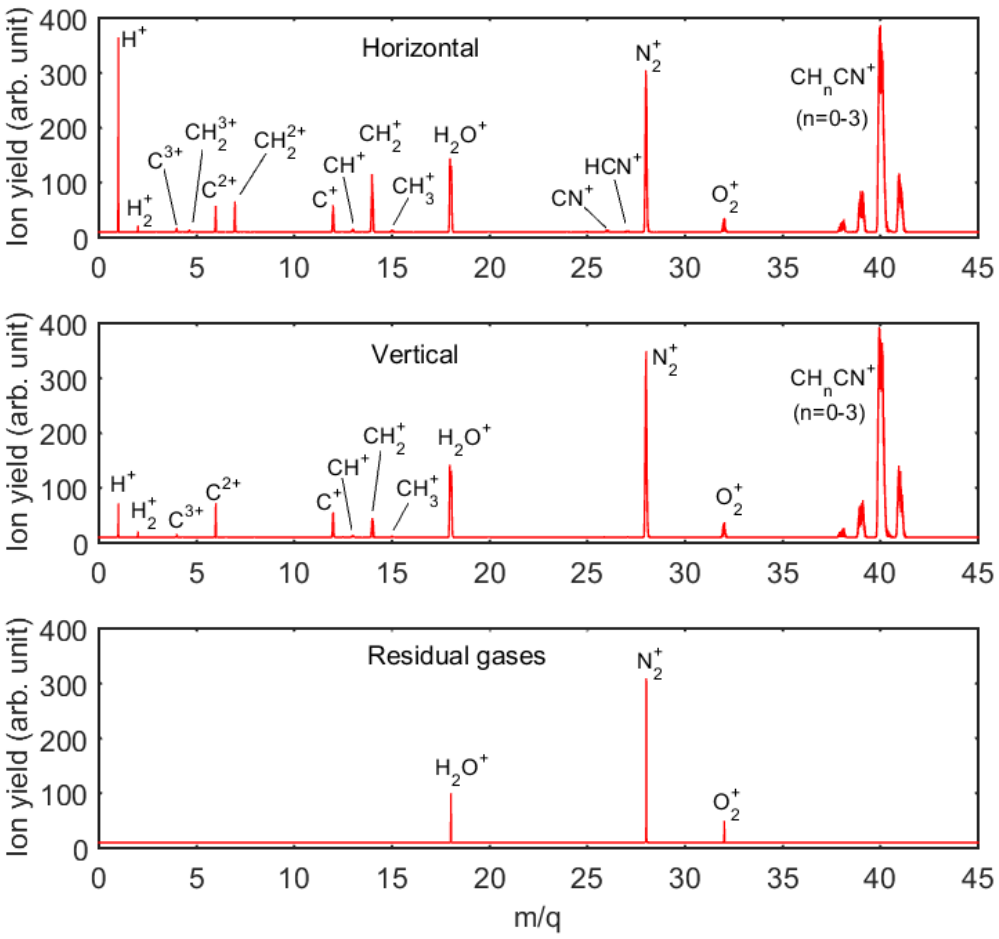

Figure 12. Upper and middle panels show TOF mass spectra for acetonitrile with horizontally and vertically polarized laser beams at the intensity of 3.3×10^{14} W/ cm^2. The bottom panel shows TOF mass spectra for residual gases with horizontally polarized light at the same intensity as with acetonitrile.

gases. The peak at *m/q* = 14 is dominated by CH_2^+, since the appearance energy for N^+, which has the same mass, is greater (33.34 eV) than the appearance energy for CH_2^+ (14.50eV) [calculated with GAMESS]. Some contribution to the N^+ peak can also come from the dissociation of residual N_2. The lowest required energy for this dissociation was found to be 24.3eV [42]. This value is high in comparison to the appearance energy of

CH_2^+. These arguments confirm our claim that the peak at m/q = 14 is presumably due to CH_2^+. Other residual gases that appear in our mass spectra are H_2O^+ and H^+ ions. The Since this value is comparatively large, we expect that the larger portion of H^+ ions in the mass spectra to originate from acetonitrile molecules and other fragments.

4.4 Angular distributions

The most noticeable feature in the yields of Figure 12 is the suppression of many ion peaks when the laser polarization is orientated vertical to the TOF axis. For this reason, we measured angular distributions of the fragment ions at the intensity of 3×10^{14} W/cm^2. A half-wave plate, with the rotation angle controlled by a LabVIEW program, was used to rotate the polarization angle of the laser beam. We measured the ion yields from 0° to 180° that are parallel to the TOF axis and for better viewing symmetrically reflected data for the angles between 180° and 360°. Although we expect left–right symmetry of these dependences, we observed slight asymmetries, which may be due to laser power variations. Figure 13 shows the measured angular dependent yield for CH_nCN^+ (n=0-3) ions. While the yield of the parent ion CH_3CN^+ is nearly completely isotropic, the ions CH_2CN^+, $CHCN^+$ and CCN^+ show an increasing degree of anisotropy with maxima at 0° and 180°, and minima at ~90° and ~270°. In order to compensate for pressure effects, each ion yield has been normalized to that of the parent ion. In Figure 13, we also fitted each fragment ion yield with $d\sigma/d\Omega = (\sigma/4\pi)[1+\sum_n \beta_n P_n(\cos\theta)]$, where $d\sigma/d\Omega$ is the differential cross section, σ is the integrated cross section, Ω is the solid angle, $P_n(\cos\theta)$ is the Legendre polynomial of order n. β is the anisotropy or asymmetry parameter. Table 2

shows the values of σ and β parameters up to 6th order as well as the maximum number of terms used in the fitting. Error bars for our data are smaller than the symbols used in the angular plots.

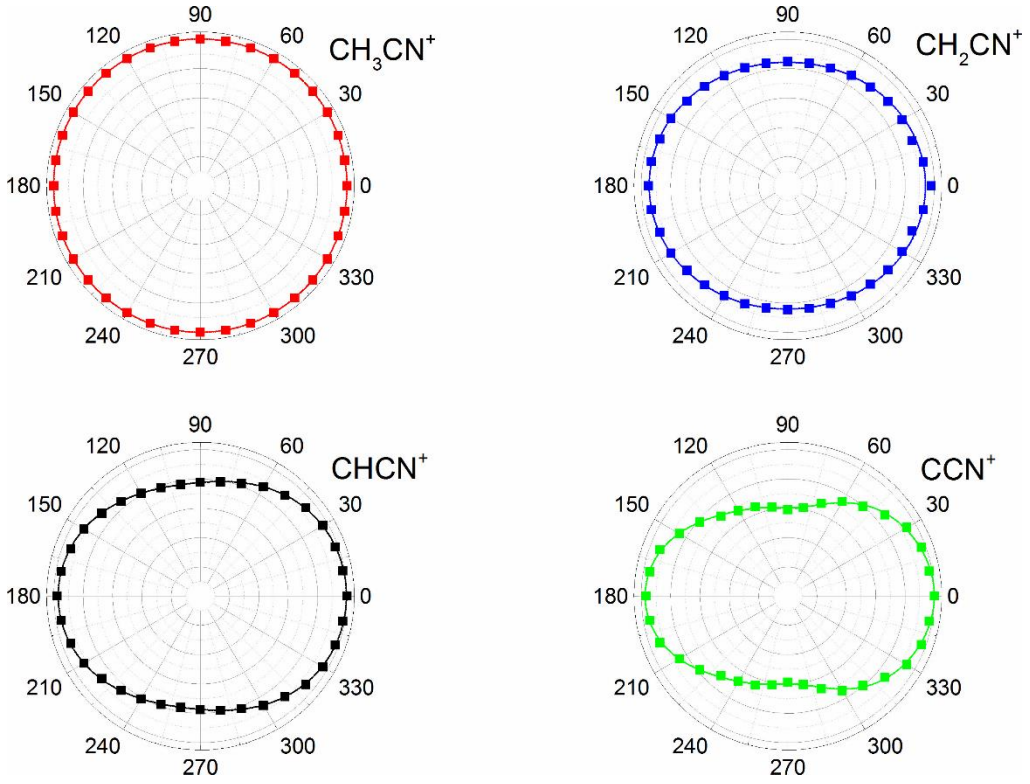

Figure 13. Angular-dependent normalized ion yields of CH_3CN^+ (red), CH_2CN^+(black), $CHCN^+$(blue), CCN^+ (green) at the intensity of 3×10^{14} W/ cm^2. Solid lines are fitted curves to the differential cross section.

Angular dependent ion yields for the lighter fragments H^+, C^+, C^{2+}, and CH_2^+ are shown in Figure 14. The fragments H^+, and CH_2^+ were found to exhibit a strong anisotropic behavior.

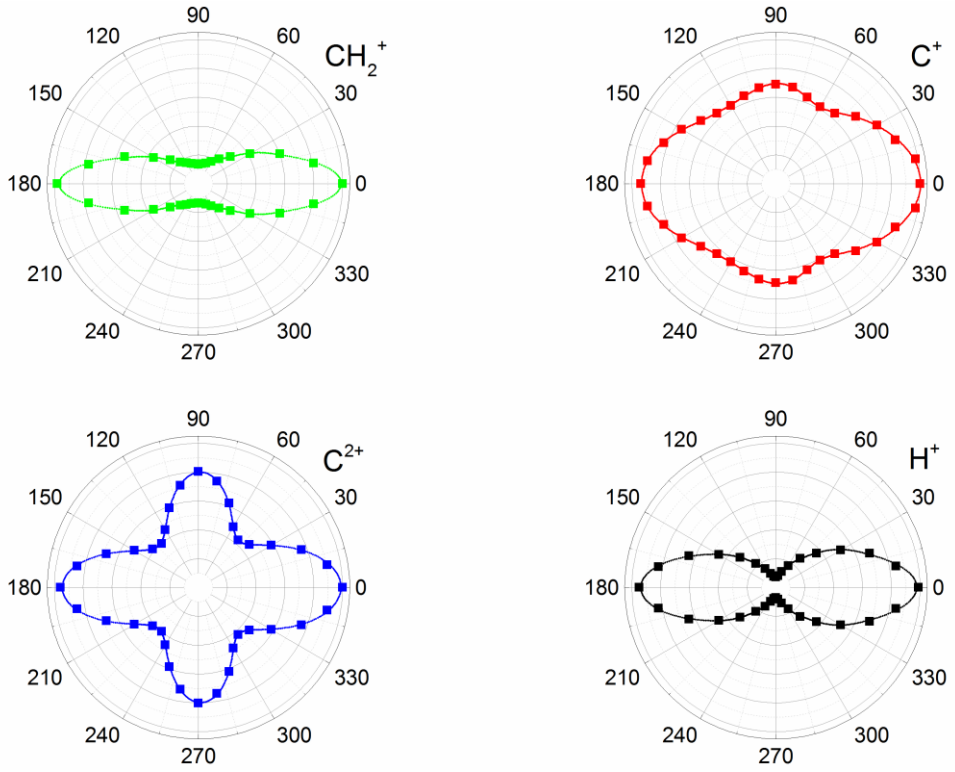

Figure 14. Angular-dependent ion yields of CH_2^+ (green), C^+ (red), C^{2+} (blue), H^+ (black) at the intensity of 3×10^{14} W/ cm^2. All the ion yields are normalized to the parent ion (CH_3CN^+) yield to cancel out pressure effects.

The indicated trend of increasing anisotropy and the reduction of the ion yields for 90º polarization can be clearly seen for these fragment ions. In particular, the strongest decreases in yields are at 90° and 270° and are observed for H^+, because they are the lightest among all the fragments. Interestingly, the angular distributions for C^+, and C^{2+} show two peaks, one for horizontal and one for vertical polarizations. This vertical yield increases as the charge state increases. The reason for the two maxima is attributed to the different locations of the carbon atoms in acetonitrile. The ions C^+ and C^{2+} most probably originate from the CCN fragment, which is obtained by removing the hydrogens from the

parent molecule CH_3CN. According to our calculations with GAMESS, to form a C^+ from CH_3CN requires high energies, i.e. the reaction

$$CH_3CN + nh\nu \rightarrow C^+ + H_2 + HCN + e^- \tag{4.1}$$

requires 17.55eV, but much less energy is needed to get C^+ from CCN molecules. This observation of perpendicular fragmentation is similar to that of Graham et. al. [43] for N^{q+} (q = 1-4) ions being ejected perpendicular to the N_2O molecule, which is similar in structure to CCN. According to their work, the peak for horizontal polarization comes from the peripheral N atom, while the vertical peak comes from the central N atom. In our case, we expect that the central C atom is responsible for the vertical peak and the peripheral C is responsible for the peak in horizontal (polarization) direction.

Table 2 Fitting parameters for each angular dependent fragment to $d\sigma/d\Omega = (\sigma/4\pi)[1+\sum_n \beta_n P_n(\cos\theta)]$.

	σ	β_0	β_1	β_2	β_3	β_4	β_5	β_6	n
H^+	0.2437	1.0000	0.1176	1.7760	0.0005	0.6257	-0.0504	0.2454	14
C^{2+}	0.5909	1.0000	0.0590	-0.1233	0.0021	0.7067	0.0161	-0.0154	10
C^+	0.6891	1.0000	0.0273	0.1881	0.0369	0.2254	-0.0067	-0.0301	10
CH_2^+	0.2395	1.0000	0.0953	1.2936	0.0426	0.8150	-0.0329	0.4310	15
CCN^+	0.7319	1.0000	0.0628	0.3478	-0.0253	-0.0065	-0.0351	0.0056	8
$CHCN^+$	0.8493	1.0000	0.0400	0.1687	-0.0235	-0.0114			5
CH_2CN^+	0.8751	1.0000	-0.0029	0.0766					3
CH_3CN^+	1.0000	1.0000							1

4.5 Intensity dependences

We have also studied the intensity dependence of photo-fragmentation of acetonitrile in the range of intensities from 4.4×10^{13} W/cm^2 to 3.3×10^{14} W/cm^2. Measurements at 50 different laser intensities were performed, while all other laser parameters were kept constant. To adjust the intensity, we used an attenuator, which consisted of a half-wave plate and a polarization cube. By rotating the half-wave plate, the polarization is changed, and since the cube polarizer transmits only the horizontal component of the polarization, the intensity was controlled in this way. Figure 15 and Figure 16 show the results of the intensity scan for acetonitrile. Under the assumption of a multiphoton mechanism of photo-dissociation, the number of photons required for each ion can be calculated by using the equation $\log(Y(I)) = \log(I^n)$, where $Y(I)$ is the ion yield, and I is the peak intensity

of the laser beam. Thus, the number $n = \log(Y(I))/\log(I)$ is just the slope of a straight line fitting to the ion yield data on a log-log scale. The fitting of the dependences with a

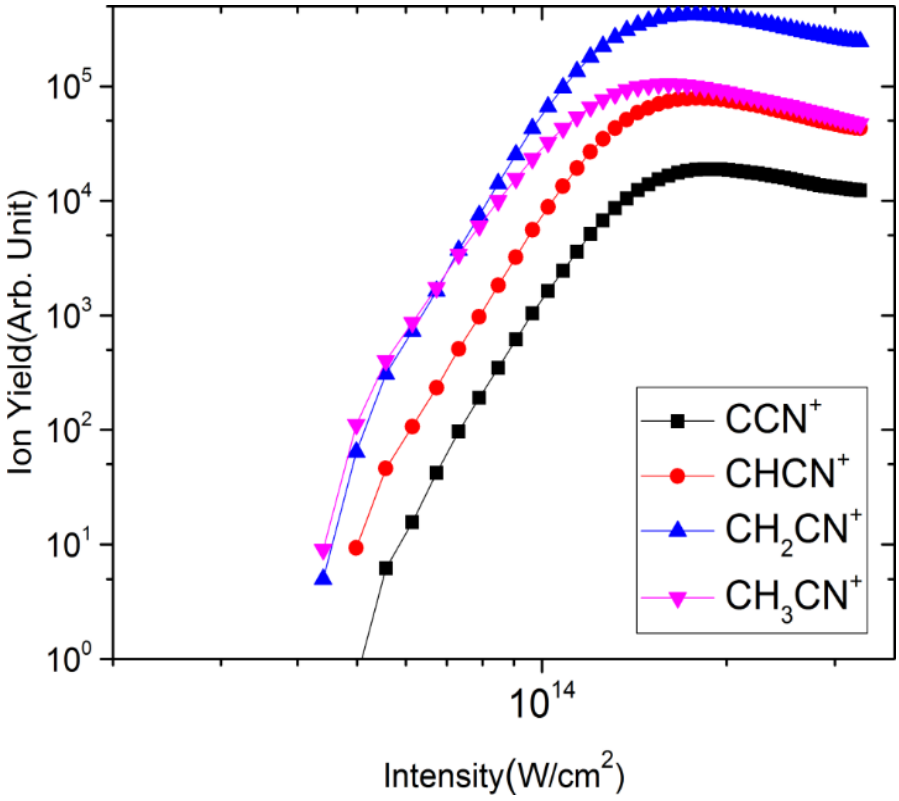

Figure 15. Intensity dependences of CH_3CN^+ (blue), CH_2CN^+ (red), $CHCN^+$ (black) and CCN^+ (green) fragment ions at the intensities between 4.4×10^{13} W/ cm^2 and 3.3×10^{14} W/ cm^2. All ions reach saturation around 1.5×10^{14} W/ cm^2 .

power-law for CH_3CN^+, CH_2CN^+, $CHCN^+$ and CCN^+ before the onset of saturation ($I \le 10^{14}$ W/cm^2) gives respectively 8, 10, 9, and 11. Because each 800 nm photon has an energy of 1.55 eV and to ionize the parent molecule takes 8 photons, we can conclude that

the ionization energy is 12.40 eV, which is close to the literature values of 12.20 eV and 12.38 eV [20, 40]. The appearance energies for other fragments: CH_2CN^+, $CHCN^+$ and CCN^+ can be obtained in the same way and give the values 15.5 eV, 13.95 eV and 17.05 eV respectively. These values compare favourably with the appearance energies found by the interaction of acetonitrile with low energy electrons [22]. This indicates that multiphoton ionization is indeed the dominant mechanism in this intensity range. This is further supported by the Keldysh parameter (between 1.536 and 0.56) for the ionization potential of CH_3CN in the same intensity range. In Figure 16, the intensity dependences for H^+, C^+, CH_2^+ and CN^+ are shown. Similar to CH_nCN^+ (n=0-3), these fragments also saturate near an intensity of about 10^{14} W/ cm^2 . The hydrogen ion H^+ yield shows an increase even at intensities higher than 10^{14} W/ cm^2 . This can be attributed to an additional contribution to the ion yield of H^+ from the residual double charged ions of H_2O. Appearance energies calculated from experimental results for H^+, C^+, CH_2^+ and CN^+ are 12.40 eV, 12.40 eV, 13.95 eV, and 12.40 eV, respectively. The results of simulations for ionization and appearance energies of the fragments can be made. All calculations were performed using GAMESS with the restricted Hartree-Fock (RHF) type calculation and 6-311G basis set. The only possible mechanism for appearance of CH_3CN^+ is

$$CH_3CN + nh\nu \rightarrow CH_3CN^+ + e^- \qquad (4.2)$$

where n is the number of required photons and $h\nu$ is the photon energy. The calculated value of 12.16 eV is in good agreement with the measured value of 12.40 eV for the process in eq.(4.2). Other calculated and experimental appearance energies are compared in Table. 3.

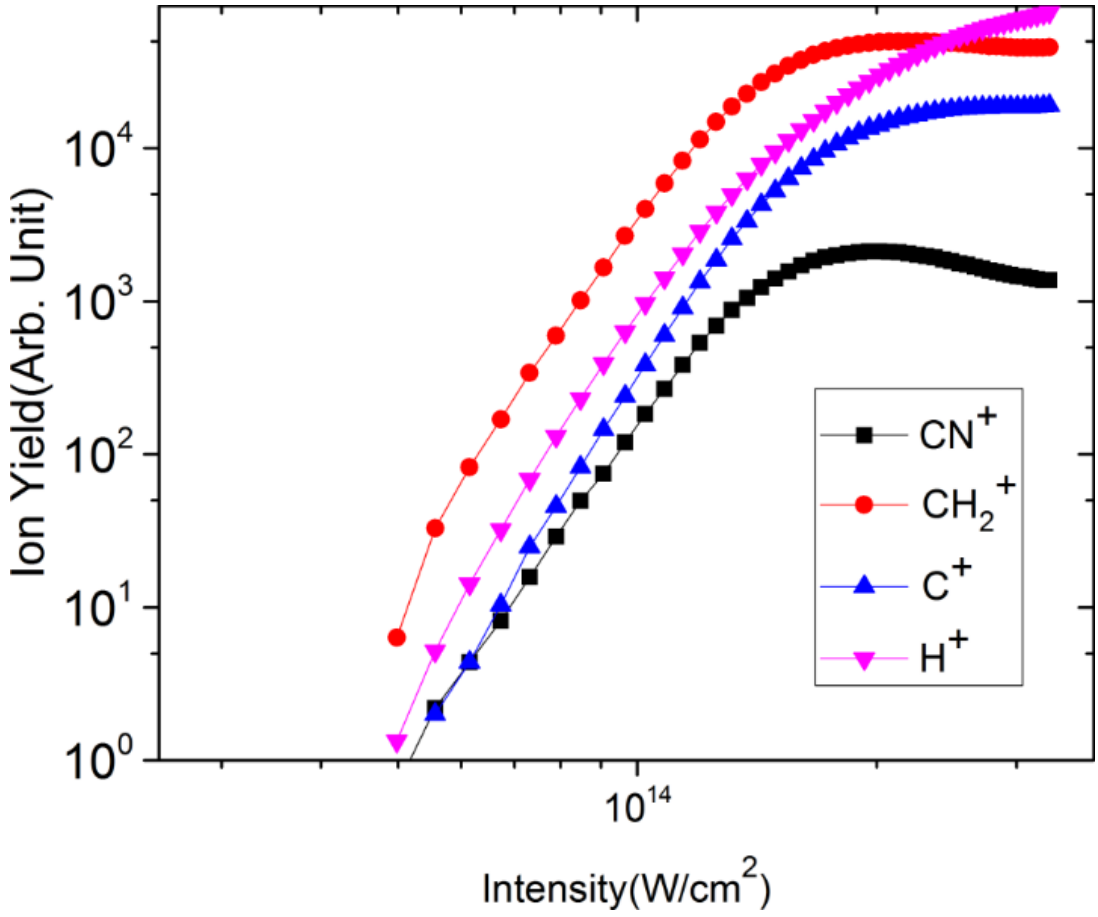

Figure 16. Intensity dependences of yields of H^+ (green), C^+ (black), CH_2^+ (red) and CN^+ (blue) fragment ions at the intensities between 4.4×10^{13} W/ cm^2 and 3.3×10^{14} W/ cm^2. All ions excluding H^+ reach saturation around 1.5×10^{14} W/ cm^2.

Table 3. Comparison of appearance energies of ionized acetonitrile and its fragments obtained by GAMESS calculations with those from experimental data.

Fragment	Reaction	GAMESS	Experiment
CH_3CN^+	$CH_3CN+nh\nu \rightarrow CH_3CN^+ + e^-$	12.16 eV	12.20 eV
CH_2CN^+	$CH_3CN+ nh\nu \rightarrow CH_2CN^+ + H + e^-$	15.77 eV	15.50 eV
$CHCN^+$	$CH_2CN+ nh\nu \rightarrow CHCN^+ + H + e^-$	14.33 eV	13.95 eV
CCN^+	$CH_2CN+ nh\nu \rightarrow CCN^+ + H_2 + e^-$	15.10 eV	17.05 eV
CH_2^+	$CH_2CN+ nh\nu \rightarrow CH_2^+ + CN + e^-$	14.70 eV	13.95 eV
C^+	$CCN^+ + nh\nu \rightarrow C^+ + CN + e^-$	14.53 eV	12.40 eV

4.6 Intensity calibration

In the study of ionization and dissociation processes, laser intensity measurements are critical. All usual detectors would be damaged when exposed to the intensity at the focal point of the laser beam, since the power density of the focal spot is very high. The intensity is also dependent of spatial pulse profile and varies with the distance from the focal spot. Because of these reasons intensity measurements are difficult. In our experiments, the intensity is calibrated using a well-known gas Xe. Since Xe has been well-studied, previous results of appearance intensities for Xe ions were used to calibrate the intensity. To do this, the mass spectrum of Xe was measured at different laser powers. The lowest laser powers required for Xe^{n+} (n=1-4) were determined. Using the results of the appearance intensities for each Xe^{n+} ion, our laser intensity was calibrated. As a result of this method, we found that our laser intensity was between 4.4×10^{13} and 3.3×10^{14} W/cm^2.

4.7 Appearance energy calculations and software

The appearance energy (or appearance potential) is the minimum energy that must be transferred to an atom or molecule to create a particular specified fragment ion. The determination of the appearance energy of any fragment is important, since it provides information to specify its neutral precursor. For instance, in a reaction

$$AB+E_{min} \rightarrow A^{+}+B+e^{-} \qquad (4.3)$$

the AB is a molecule consisting of atoms A and B. AB dissociates into positive ion A^{+} that is a result of ejection of an electron and a neutral atom B after E_{min} is absorbed. Here E_{min} is the minimal energy introduced into molecule to observe certain fragment. In order to calculate the appearance energy, the energies corresponding to each term in the reaction need to be known. The total energies on the right side and left side of the reaction must be the same. In the assumption that the kinetic energies of fragments are negligible the energy difference that is found with GAMESS calculations will give the minimal required energy for appearance of A^{+}, which should be expected to be close to the experimentally determined value of E_{min}. In the following section, methods and software used to calculate the appearance energies will be discussed.

4.7.1 Experimental method

In order to determine the appearance energy of fragments, intensity dependent ion yields for each fragment were measured as we discussed above. Slopes of the straight segments were determined using the log-log scale (Figure 17). The slope values are the minimum number of photons for a fragment to appear. Since a photon energy for 800nm wavelength

is 1.55 eV, simply multiplication of the slope value by one photon energy gives the appearance energy. For example, the slope value for CCN^+ was determined as 11 which means appearance energy of CCN^+ is 17.05 eV. These procedure was done for each fragment and experimental values, which were given in Table 3 were determined.

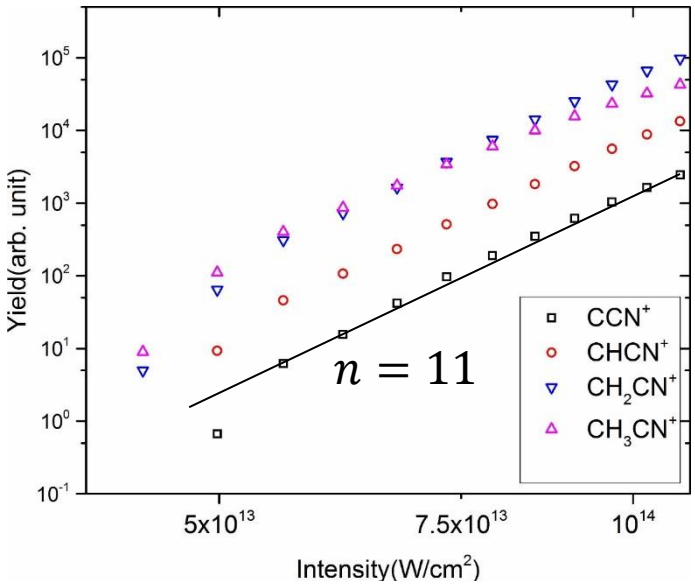

Figure 17. Intensity dependent ion yields on a log-log scale.

4.7.2 Theoretical calculation method using GAMESS

GAMESS is an abbreviation for General Atomic and Molecular Electronic Structure System that is a computational software program capable to perform wide range of quantum chemistry computations such as Hartree-Fock (HF), density functional theory (DFT), and multi-configurational self-consistent field (MCSCF). It was developed by the research group at Iowa State University, and it is a free software. In order to perform any kind of computations an input file needs to be generated. This input file should include

three basic inputs that are optimized molecular structure, the basis sets, and the theory (type of wave function), which are essential for all computations. In our work, RHF method and 6-311G basis set have been used to get more accurate results. Input files were created with these options by using the software program Avogadro. After GAMESS is run with the input file it creates an output file (.log file). This is a text file which involves all the results for the computation. Energy of the atom or molecule are included in the file in hartree unit (1 hartree is equal to 27.211 eV). These energies are converted to electron-volt and appearance energies are calculated for desired fragments in unit of eV.

As an example, energy for CH_3CN was found to be -131.9613212518 Hartree and for CH_3CN^+ the energy was determined as -131.5145201299 Hartree. The reaction for this can be written as

$$CH_3CN + E_{\min} \rightarrow CH_3CN^+ + e^- . \qquad (4.4)$$

Since energy is conserved, energies of the right side and left side should be equal, so that the energy difference will give the value for $E_{\min}$. The energy difference for the given example is 0.4468011219 Hartree (12.16 eV). Similarly, appearance energies for other fragments were also calculated.

4.7.3 Avogadro software

Avogadro is an advanced molecular editor and visualization tool, which can be used for molecular building and computational chemistry. Chemical data can be extracted in a wide variety of formats, including. inp files that is suitable to run with GAMESS. Molecular structure is important, since it affects the chemical and physical properties of the molecule,

so that geometry optimization needs to be done when quantum chemical computations are performed. Avogadro has been used to model the acetonitrile and other fragments, and also to optimize their geometry. An image of molecular structure of acetonitrile created by Avogadro is shown in Figure 18. Input files created by Avogadro were sent to the GAMESS program to compute the energy of each neutral and singly charged atoms and molecules that are expected to be formed after dissociation of acetonitrile.

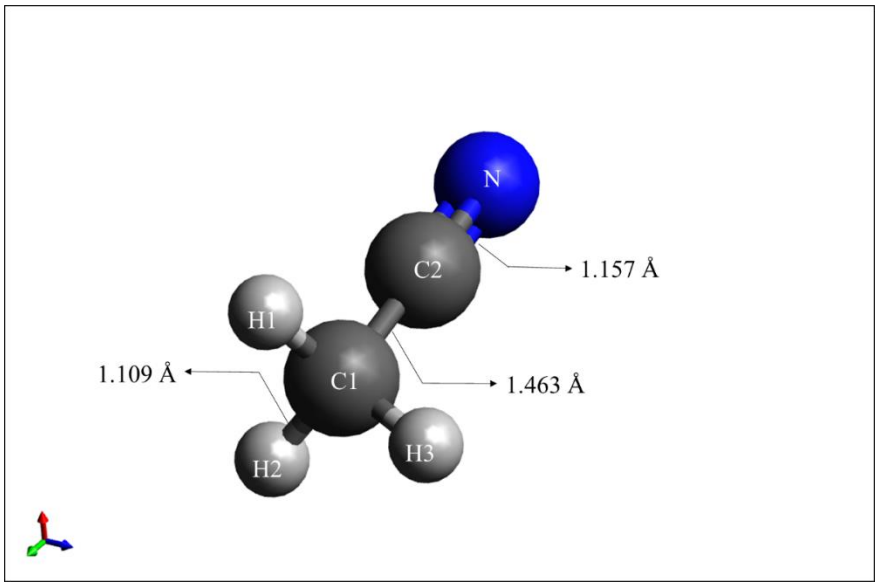

Figure 18. Molecular structure of the acetonitrile molecule created by Avogadro software.

4.8 Conclusions

We have performed a detailed experimental study of the ionization and dissociation of acetonitrile (CH_3CN) using RTOFMS at different laser irradiation conditions. We have first measured the mass spectrum of acetonitrile at different laser polarizations, which showed different amplitudes for certain fragments such as H^+ and CH_2^+. These differences brought an idea to measure the angular dependence of each fragment ion. We have seen that some fragments show isotropic behavior, and some fragments show anisotropic behavior. Interestingly, the fragments C^+ and C^{2+} showed two maxima; one is for horizontal and one is for vertical polarization. Different location of C atoms causes ion yields of C^+ and C^{2+} to exhibit two peaks in the TOF directions parallel as well as perpendicular to the polarization direction.

We also studied intensity dependences of fragment ions ejected from acetonitrile in the intensity range from $4.4\times10^{13}\,\mathrm{W/cm^2}$ to $3.3\times10^{14}\,\mathrm{W/cm^2}$. Using these experimental results, appearance energies were obtained. In order to confirm our results, we have made quantum chemical calculations using a free software GAMESS. Experimental results and theoretical results obtained from GAMESS were compared. Power dependences of fragment ions show that the fragments appear as a result of a multiphoton process, and consequently, from the slopes of the dependences of the fragment yields on intensity the minimal number of the required photons and the appearance energy can be evaluated.

CHAPTER V

KINETIC ENERGY RELEASES OF PROTONS EJECTED FROM ACETONITRILE[2]

5.1 Introduction and theory

Laser induced ionization and dissociation of polyatomic molecules have been the subject of several experiments. One of the interesting questions in these experiments is the determination of the kinetic energy releases (KER) of the protons ejected during the dissociation. Proton energies ejected from small and large hydrocarbon molecules [44, 45] have been studied at moderate laser peak intensities. Experimental studies on KERs of protons ejected from polyatomic molecules have concentrated not only singly charged and neutral but also multiply charged fragments where also Coulombic repulsion occurs. KER of protons is depend on the molecular structure and the laser intensity [46]. In this section, KER of protons ejected from acetonitrile and their dependences on laser polarization and laser intensity has been investigated using the LTOFMS.

5.1.1 Coulomb explosion

Coulomb explosion process under intense laser radiation was first observed by Frasinski and Codling in 1987 [47]. As a result of Coulomb explosion, single and multiply charged fragments are originated with different kinetic energies and these fragments carry a lot of necessary information to understand the interaction of molecules and an intense laser light.

---

[2] Part of this chapter is reprinted with permission from "Dissociative ionization of acetonitrile in intense femtosecond laser fields." by Y. Boran, A. A. Kolomenskii, M. Sayrac, N. Kaya, H.A. Schuessler and J. Strohaber. J. Phys. B: At. Mol. Opt. Phys. 50 (2017) 135003. doi.org/10.1088/1361-6455/aa6f52,

At high laser intensities, several electrons from the molecule can be removed rapidly which causes to form multiply charged ions. These highly charged molecular ions can explode because of the Coulomb repulsion of particles having the same electric charge. This phenomena is called as Coulomb explosion and has been studied for both polyatomic [14, 29] and diatomic [48, 49] molecules. In the case of diatomic molecules, the Coulomb explosion energy is expressed by $Q_1.Q_2 / \mathrm{R}_e$ (atomic unit) [50], where Q_1 and Q_2 stands for atomic ion charges and R_e is the inter-nuclear separation at equilibrium.

When the laser polarization is parallel to detection axis of the TOFMS, the ion peaks originated via Coulomb explosion appear as pairs on the both side of the central mass or as a broad peak on the mass spectra because of the backward and frontward ejected fragments. While frontward ejected fragments are accelerated more, backward ejected fragments are first decelerated and change the direction of motion and then accelerated. Backward and frontward ejected ions having the same mass to charge ratio cause arrival time differences resulting peak splitting or broadening.

5.1.2 Field assisted dissociation

The Coulomb explosion model is widely accepted to interpret the dissociation mechanism. This model assumes that two or more electrons are removed from the molecule resulting in a dissociation. However, at the moderate laser intensities, it is not easy to remove two or more electrons from the target molecule and the Coulomb explosion model cannot be used to understand the dissociation processes. Two models have been used to explain the dissociation of diatomic molecules introduced by Dietrich and Corkum [51] and Thachuck

and Wardlaw [52]. Polyatomic molecules have not been studied extensively as have those of diatomic molecules. Therefore, there has been no suitable model for polyatomic molecules. Recently, a model which is called field- assisted dissociation (FAD) was developed by X Tang and co-workers [12]. FAD model assumes that in the presence of strong laser field, the inter-nuclear distance of a specific bond, whose axis is parallel to the laser field, is taken into consideration and rest of the molecular geometry is fixed. In this case, the molecule can be thought as a diatomic molecule. The inter-nuclear distance is strongly adjusted with laser field oscillations. If the laser field is on, the bond length increases, which results in that chemical bond to be softened. When laser intensity is strong enough and laser pulse duration lasts long enough, that bond can be pulled off. Contrary to the Coulomb explosion model, this process could be considered as a laser field assisted dissociation of the molecule.

5.1.3 Quasi-equilibrium theory (QET)

One of the theoretical approach for explaining the dissociation of molecules is the quasi-equilibrium theory. QET is the extension of RRKM (Rice-Ramsperger-Marcus-Kassel) theory and it was first introduced by Rosenstock in 1952 [53]. This theory gives a physical description of the mass-spectral behavior and that has been widely accepted and used so far. When a molecule is ionized, the excited molecular ion is produced without any change in the bond length since ionization occurs very fast. Excluding the small molecules, transitions between energy states are adequately fast such that a quasi-equilibrium among these energy states is created before dissociation of ionic molecule takes place. For this reason, dissociation of ionic molecule is only depending on the internal energy and the

molecular structure. The dissociation rate of the molecular ion is determined by the probability of the randomly distributed energy over the molecule. If this energy is concentrated in a particular bond, this bond can be broken. A fragment ion can further dissociate, if initial molecular ion has enough energy.

5.2 Experimental method

To gain further insight into the mechanisms associated with the appearance of different ion species, the kinetic energy release (KER) of H^+ ions generated from CH_3CN was measured using the direct path TOF mode of the spectrometer. In this mode of operation, the voltages on the ion mirror were set to zero, and a small potential was applied to the repeller plate to allow ions having different kinetic energies to arrive at MCP2, located at the back side of flight tube (Figure 5), at different times. Other than that, experiments have been performed at the same conditions (pressure, intensity, pulse duration, wavelength etc.) as in the previous section.

5.3 Angular distributions and intensity dependences of protons

Angular distributions of H^+ ions were measured using the same method as discussed in the previous chapter. A two- dimensional plot of H^+ ion yields as a function of the time-of-flight and polarization angle is shown in Figure 19, and corresponding polar plots are shown in Figure 20. In this data, we observed three different peaks for the H^+ ions suggesting that not all of the H^+ ions originate from the same physical mechanism. In Figure 19, the peak labelled QET is located around ~9.4 μs and is seen to be independent

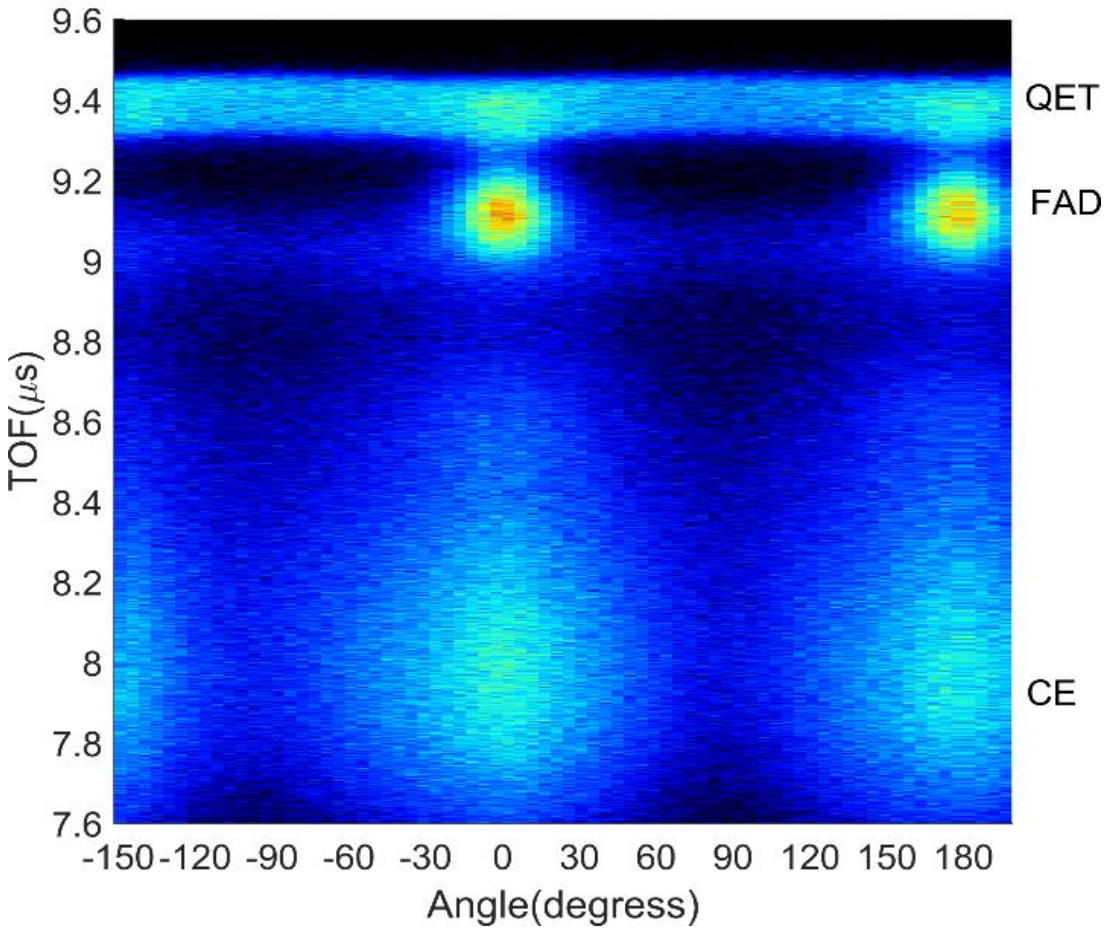

Figure 19. TOF of H^+ as a function of laser polarization using direct time-of-flight path.

of the polarization angle. The peak labeled FAD appears around ~9.1 μs and strongly peaks when the polarization is along the TOF axis. The peak appearing around ~8.0 μs and labeled CE is polarization dependent and broader in time. The polarization independence of the QET peak on the top in the Figure 19 is attributed to quasi-equilibrium

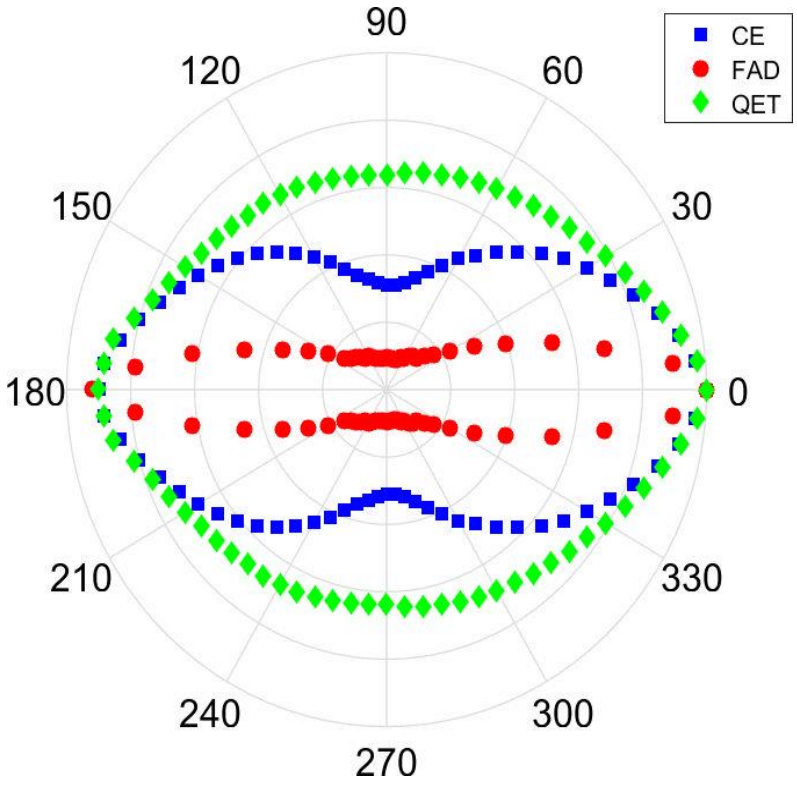

Figure 20. Corresponding angular distributions for each mechanism in Figure 19 are shown in polar plots.

theory (QET) or the Rice–Ramsperger–Kassel–Marcus (RRKM) dissociation mechanism [54]. According to these theories, after a molecule has been ionized, the new potential energy surface is different from the initial potential energy surface and the system is left in an excited state. Excess energy from these 'hot' molecules is redistribution among the various internal degrees of freedom and can result in dissociation. A characteristic of this type of dissociation is that it is described statistically, which means dissociation is independent of the polarization. The peak labelled FAD shows maxima in the polarization at 0° and 180°, and minima at 90° and 270°. These peaks are attributed to field assisted dissociation (FAD). In the FAD mechanism, the laser field is considered large enough

such that it can sufficiently distort the potential energy curve along a bond axis thereby effectively "pulling off" a chemical bond. This mechanism strongly depends upon the laser polarization and results in a small kinetic energy release. The peak labeled CE has a broad TOF distribution compared to the other peaks and shows an angular dependence similar to the FAD peak. The broad distribution and angular dependence of the peak indicates that these ions originate from Coulomb explosion (CE).

As discussed above, it is expected that Coulomb explosion occurs at larger intensities, while dissociation following QET occurs at lower intensities. In Figure 21, the intensity dependent yields of H^+ for each processes are shown. This data depicts that the peak associated with QET has the lowest appearance intensity similar to the appearance intensities of the singly charged ion, where MPI is known to be the dominate ionization mechanism. This is followed by the FAD peak and the CE peak. The CE peak has a larger appearance intensity and is near that of the doubly charged species. The order in which the yields appear on the intensity graph supports our claim that the H^+ ions are coming from different processes. A similar observation was first observed by Strohaber at. al., in the dissociative ionization of methane.

5.4 KER calculations and determination of the focal position in the interaction region

In order to determine the kinetic energy of the measured H^+ ions, the TOF as a function of focal position in the acceleration region was calculated for frontward and backward ejected ions using Newton's 2nd law,

$$t_{\text{lin}} = \sqrt{\frac{M}{Q}}\sqrt{\frac{x_R}{V_R}}\left(\frac{2x_0 + L + v_0^{\,2}/a}{\sqrt{2x_0 + v_0^{\,2}/a}}\right) \pm \frac{v_0}{a} \tag{5.1}$$

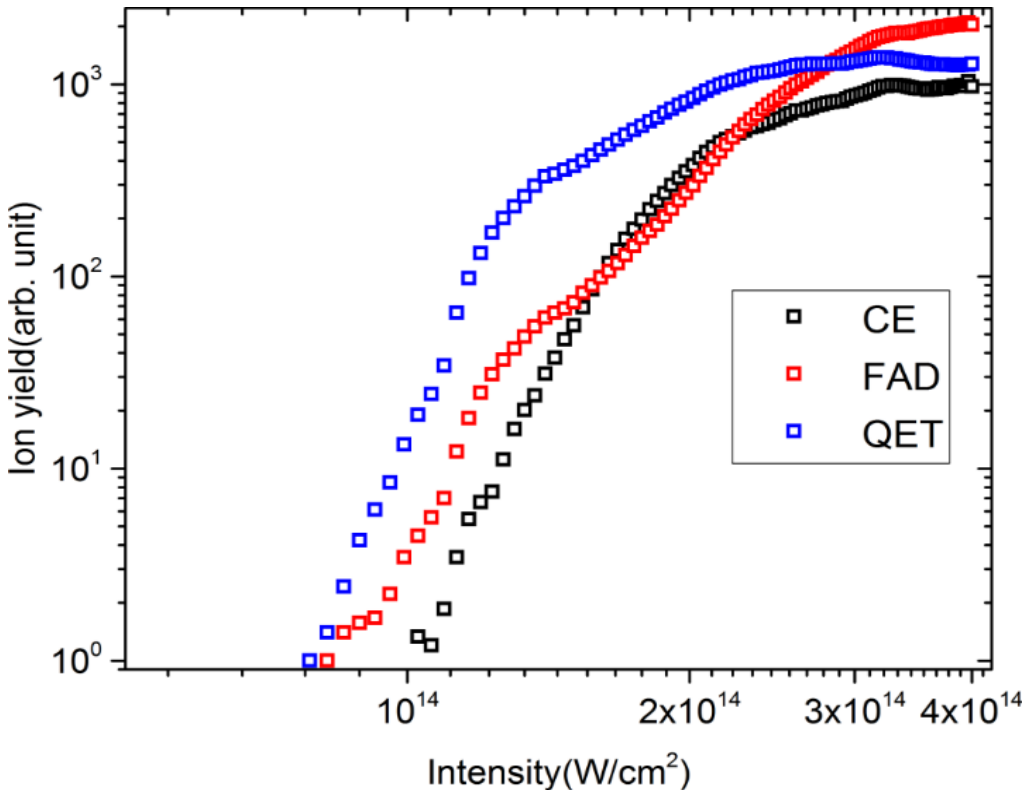

Figure 21. Intensity dependences of H^+ yields. Yields for three different processes are shown. Coulomb explosion (CE, black), Field assisted dissociation (FAD, red), and quasi-equilibrium theory (QET, blue).

Here M and Q are the mass and charge of the ion, L is the length of flight tube, x_R is distance between repeller plate and slit plate, x_0 is the focal position, V_R is the potential on repeller plate, and $v_0 = c\sqrt{2KE/mc^2}$ is the initial velocity. The TOFs for $KE = 0$, $KE = 3\text{eV}$, and $KE = 15\text{eV}$ are plotted in Figure 22 using Eq. (5.1) . In the case of zero initial kinetic energy $KE = 0$, the dependence of Eq. (5.1) is shown by the solid red curve

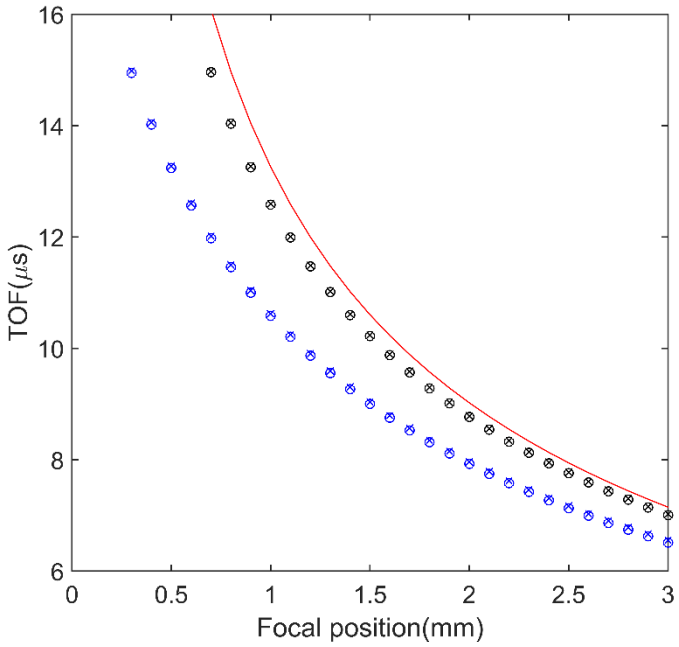

Figure 22. TOF of H+ with different kinetic energy releases. 0 eV (red), 3 eV (black), 15 eV (blue). Circles and crosses show TOF of frontward and backward ejected H^+.

in Figure 22. For the case where $KE = 3\text{eV}$, Eq. (5.1) gives the black circles and crosses shown in Figure 22. The circles represent the forward directed fragments and the crosses

represent the backward directed fragments. Similar data is shown by the blue circles and crosses for a kinetic energy of $KE = 15\text{eV}$.

In order to determine the initial kinetic energy of the hydrogen ions from their TOF in the measured spectrum, the position of the focus in the acceleration region must be determined. This can be accomplished by solving Eq. (5.1) for position x_0. If we set $v_0 = 0$ the expression (5.1) can be written in the form of quadratic equation as following;

$$4{x_0}^2 - 2\left(\frac{t_{lin}^2 V_R}{x_R}\frac{Q}{M} - 2L\right)x_0 + L^2 = 0 \tag{5.2}$$

Solving the Eq. (5.2) for x_0 gives,

$$x_0 = \frac{1}{2}\left(\frac{t_{lin}^2 V_R}{2x_R}\frac{Q}{M} - L\right) \pm \sqrt{\left(\frac{t_{lin}^2 V_R}{2x_R}\frac{Q}{M} - L\right)^2 - L^2} \tag{5.3}$$

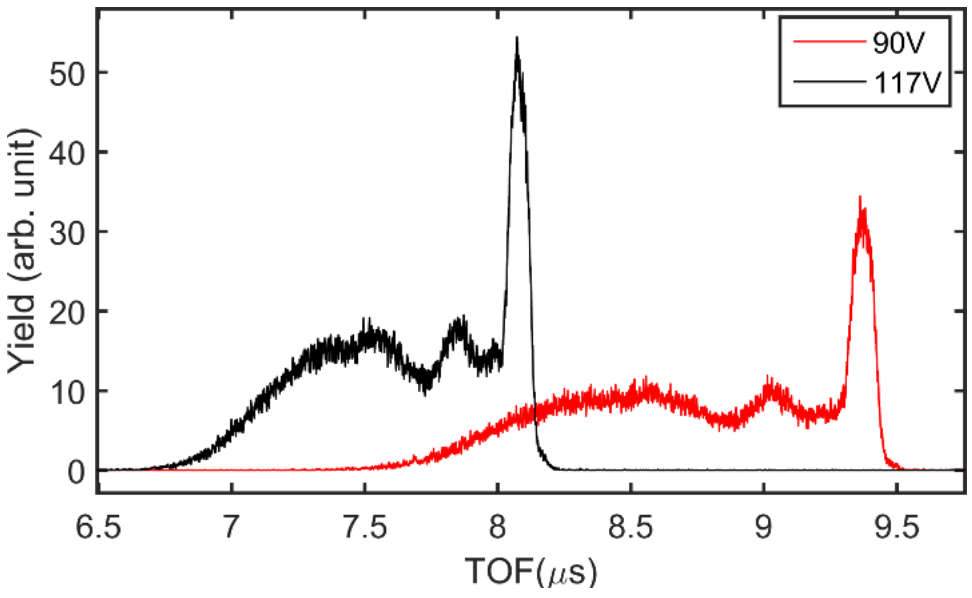

Figure 23. TOF of H^+ ions obtained with linear part of TOFMS using 90V (red) and 117V (black) on repeller plate.

Since it is difficult to measure the position of the focal point between the repeller and slit plates, two different potentials were applied to the repeller plate and the yields were measured using the same peak intensities (Figure 23), which allowed the position of the focus to be double checked. When a higher voltage is used, ions arrive at the detector earlier and the peaks become narrower. The time difference between the two QET peaks is around $1.3\mu s$. Inserting all relevant quantities into Eq. (5.3), we find that the focal position x_0 is equal to 1.868mm for 90V and 1. 864mm for 117V giving an average focal position of 1.866 ± 0.002 mm.

5.5 Gaussian fits to TOF peaks and KER calculation method

Using the focal position that we have found in previous section, a list of TOFs for H^+ ions was calculated using a list of kinetic energy from 0-30 eV. Gaussians were fitted to each

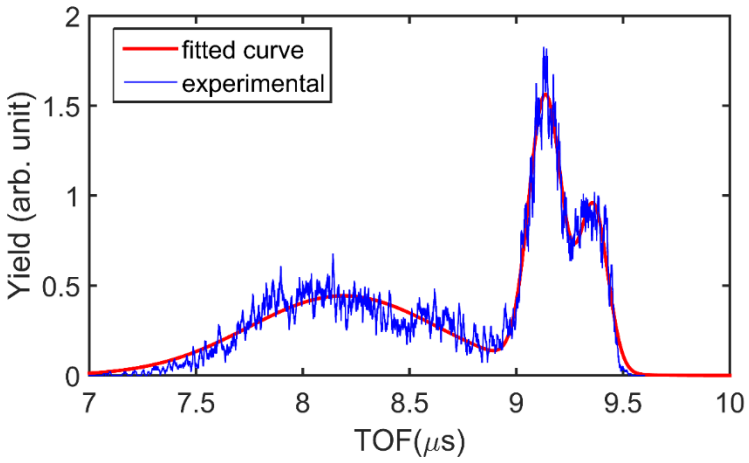

Figure 24. TOF of H^+ ions obtained with linear time-of-flight path using 90V (blue) and Gaussian were fitted to the H^+ peaks (red).

peak to find the TOF positions for different intensities (Figure 24). Kinetic energies corresponding to each position were found using the interpolation method in MATLAB. Kinetic energy release as a function of intensity are shown in Figure 25. This figure indicates that the KER of H^+ formed via CE increases with increasing laser intensity from about 9 eV to 15 eV. This trend is consistent with reported kinetic energy release of H^+ formed from propane(C_3H_8) [14]. The explanation is that as the intensity increases ionization occurs earlier and at a smaller inter-nuclear separation distance resulting in a larger Coulomb force and therefore a larger CE. The middle peak shows a smaller increase in KER while the first peak shows no change with increasing intensity. In [55] the first peak is attributed to bond softening and the second peak is attributed to above threshold dissociation. In that paper, KER of these two peaks decreases with the increasing intensity, but in our results KER of these peaks shows a different trend. KER of FAD peak is increasing while the KER of QET peak is not changing. These results further support our claims that the first and second peaks are most likely not originated from bond softening and above threshold ionization, but they are coming from QET and FAD.

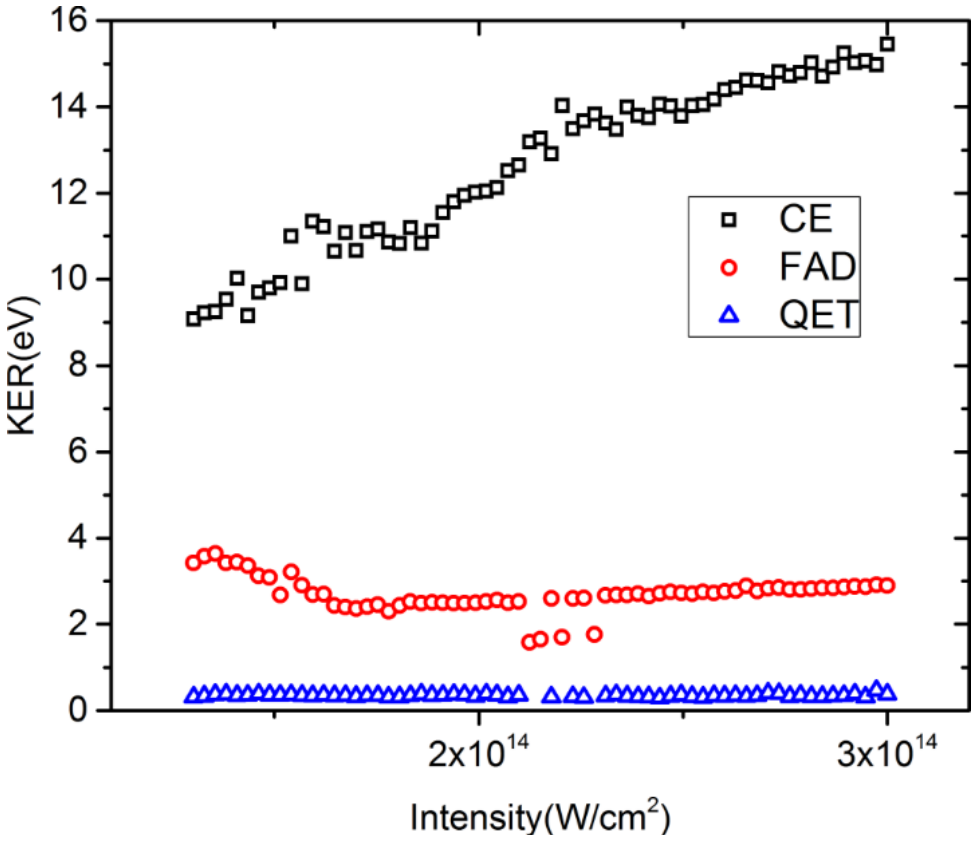

Figure 25. Measured KER of H^+ ions as a function of intensity for different processes. Coulomb explosion (CE, black), Field assisted dissociation (FAD, red), and quasi-equilibrium theory (QET, blue).

5.6 Conclusions

We studied kinetic energy releases of protons ejected from acetonitrile molecule using the linear part of the TOFMS. The results showed that H^+ ions are originated via different mechanisms. The properties of these mechanisms were further investigated by measuring the angular distributions and intensity dependences. We developed an equation to calculate the kinetic energies of protons having different initial velocities. We also used Gaussian function to TOF peaks to find the center position of each peak at different

intensities which is essential to find the peak shifts with the changing intensity. The kinetic energy releases of H^+ provide evidence that at least three different dissociation processes are involved: Coulomb explosion, field assisted dissociation, and Quasi-equilibrium theory dissociation.

CHAPTER VI

KINETIC ENERGY RELEASES OF HYDROGEN SPECIES EJECTED FROM ETHANE

6.1 Introduction

In previous chapter, we measured kinetic energy releases of H^+ ion formed through dissociation of acetonitrile. The results showed that H^+ ions are originated via different mechanism. In this aspect, kinetic energy releases of hydrogen ions formed via different molecules can be also measured if other mechanisms are involved to form the H^+ ion. In addition to H^+, kinetic energy releases of H_2^+ and H_3^+ would also provide some useful information.

The dissociation and ionization of hydrocarbons has attracted considerable interest in last decades [56, 57]. In hydrocarbons, hydrogen atoms have high mobility so that a variety of ionic species can be formed not only due to breaking the bond but also hydrogen migration. In this respect, one of the well investigated molecular system is ethane [58, 59]. Ethane (C_2H_6) is the simplest saturated hydrocarbon next to methane and consists of two carbon and six hydrogen atoms. The dissociative ionization of ethane results in formation of atomic hydrogen, diatomic hydrogen and $C_2H_n^+$, $C_2H_n^{2+}$ (n=0-6). In addition to these fragments, the dissociative ionization of C_2H_6 leads to the production of a rather interesting fragment ion H_3^+. The H_3^+ is one of the crucial chemical species in interstellar chemistry, since in ion-molecule reactions it acts as a significant proton transfer reactant. Therefore, it is intriguing to study formation of H_3^+. The first observation of H_3^+ under intense laser pulses was most probably achieved by Xia et al [50]. In this study, the peak

at m/z=3 was considered as C^{4+}, but it was most likely H_3^+, considering today's knowledge. In this chapter, KER of hydrogen species formed from ethane and their dependences on laser intensity and laser polarization have been studied using the LTOFMS for better understanding of formation mechanisms of these hydrogen species.

6.2 Experimental details

In order to understand the formation of the hydrogen ion species, kinetic energies of each hydrogen ion species were measured experimentally. TOFMS was operated in linear mode similar to previous measurement of acetonitrile. The voltage on the repeller plate was kept at small voltage (90V) and the voltages on the grids were zero (V_1=V_2=V_3=0). By using these settings, we were able to separate the ions having different kinetic energies in the TOF spectrum. The TOF chamber was evacuated to the pressure of $\sim 5\times10^{-9}$mbar, and ultra-high purity ethane gas from Matheson company was introduced into the ionization region through a leak valve. When the pressure was stabilized around 5×10^{-7}mbar, measurements were performed for angular distributions and intensity dependences. Intensity and polarization of the laser beam were controlled by using halfwave plate and cubic polarizer. In these experiments, laser parameters were the same as acetonitrile measurements.

6.3 Experimental results and discussion

TOF spectrum of atomic, diatomic and triatomic hydrogen ions were measured using horizontal and vertical polarizations. The comparison of the TOF spectrum with two different polarizations are shown in Figure 26. Four distinct peaks and one sharp peak

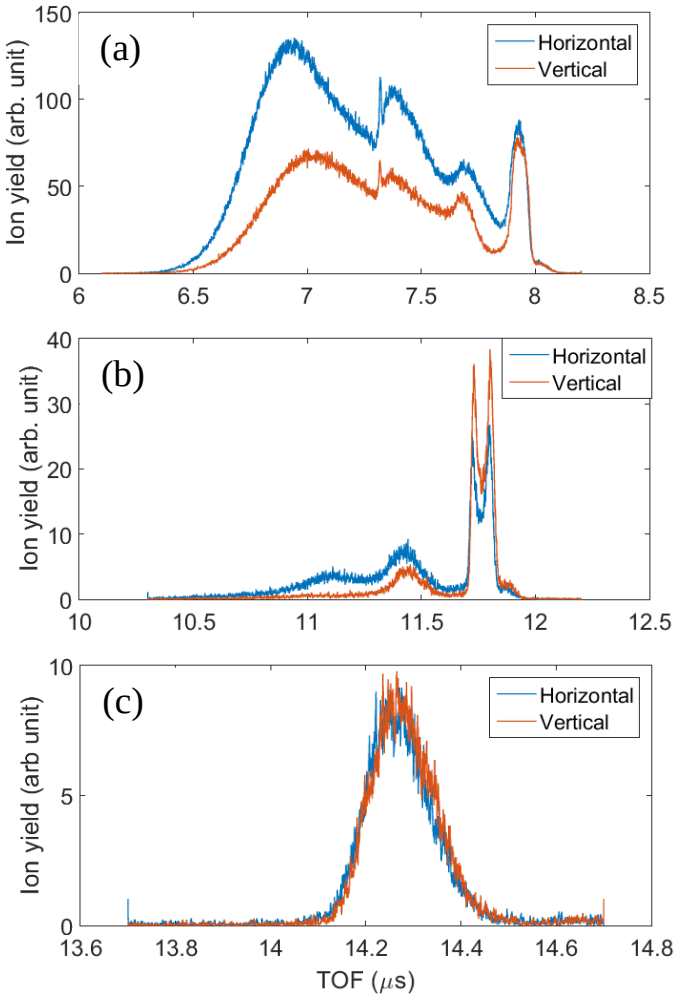

Figure 26. TOF spectrum of (a) atomic H^+, (b) diatomic H_2^+, and (c) triatomic H_3^+ hydrogen ions at the intensity of $\sim 4\times10^{14}\mathrm{W/cm^2}$ in the ionization of C_2H_6. The orange color shows vertical polarization and blue color presents horizontal polarization.

were observed for H^+ ions. In chapter 5, TOF spectrum of H^+ also showed that various mechanisms are responsible for the formation of atomic hydrogen in the ionization of CH_3CN. We observed there different humps in the TOF spectrum of H_2^+, but H_3^+ consists

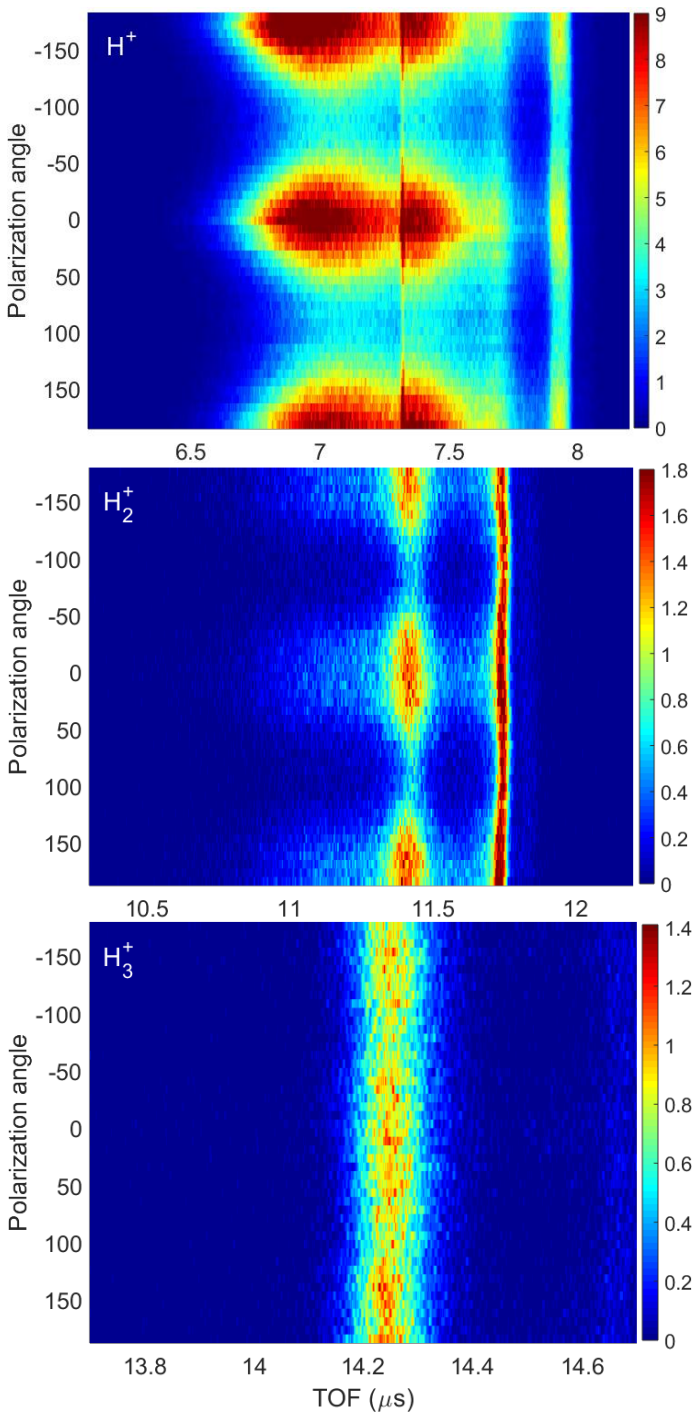

Figure 27. Color density plots showing the angular distributions of H^+, H_2^+ and H_3^+ at the intensity of $4\times10^{14}\,\mathrm{W/cm^2}$.

of only one peak. When polarization direction is changed from horizontal to vertical, some of the peaks are suppressed while others are not affected.

In order to see how hydrogen species are changing with laser polarization and laser intensity, we performed angular scans from 0 to 360 degree, and intensity scan from 1×10^{14} and 4×10^{14}W/cm^2 by using the TOFMS in linear mode. Experimental results of polarization and intensity dependences are shown in Figure 27. For H^+, first and second peaks exhibit strong laser polarization dependence having maxima at 0 and 180 degrees and minima at 90 and 270 degrees. However, the third and second peaks for H^+ slightly depend on the laser polarization. The first and second peaks for H_2^+ are strongly depend on the polarization direction, while the third peak is independent of the laser polarization. The H_3^+ peak is almost independent of the laser polarization as it stays the same when polarization is altered from 0 to 360 degrees. In Figure 28 intensity dependences of hydrogen species for each peak are presented. As can be seen all hydrogen ions are originated at around similar intensities. Low energetic peaks are dominating at lower intensities while high energetic peaks are prevailing at the higher intensities for H^+ and H_2^+. Different appearance intensities for each peak support that H^+ and H_2^+ are arising from different mechanisms.

We also calculated kinetic energies of measured hydrogen ion species using Eq. (5.1). In order to calculate the kinetic energy of each peak for hydrogen ion species, the position of each peak needs to be known. To do this, the sum of four Gaussians for H^+, the sum of three Gaussians for H_2^+ and one Gaussian for H_3^+ were used to fit the data. The

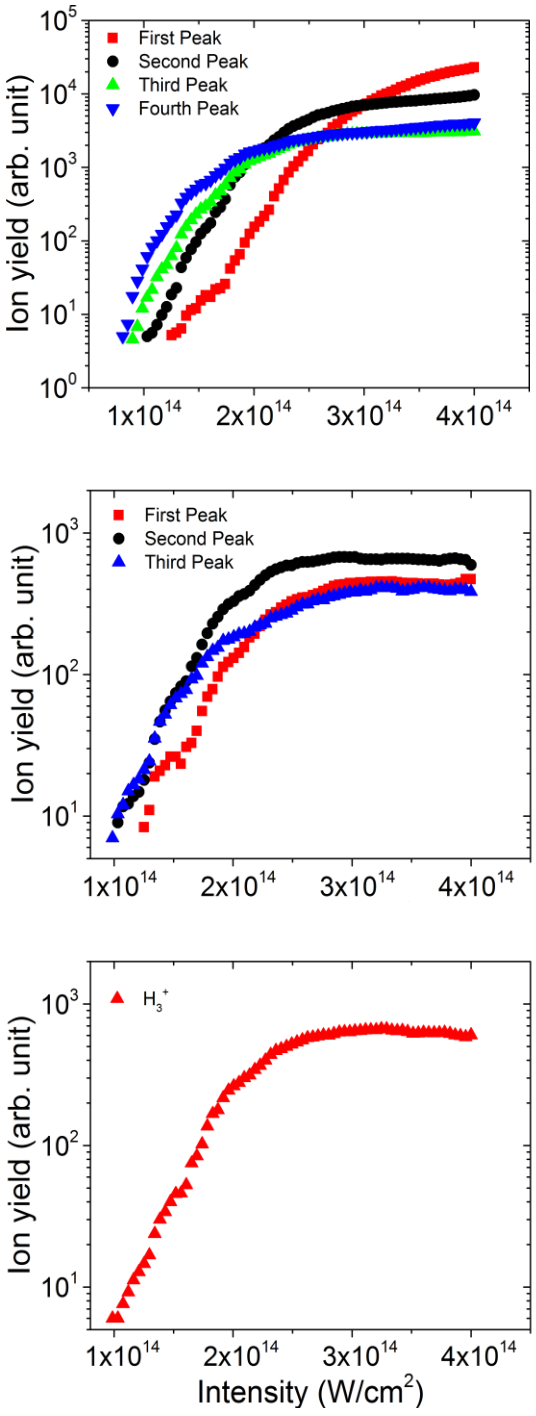

Figure 28. Intensity dependences of atomic (upper panel), diatomic (middle panel) and triatomic (lower panel) hydrogen measured between 1×10^{14} and $4\times10^{14}\mathrm{W/cm^2}$.

fitting curve for H^+ is presented in Figure 29. Using a MATLAB code, center positions of each Fitting curve is presented in Gaussian curve for each intensity were listed. Kinetic energies corresponding to center positions of the Gaussians were calculated using the interpolation method in MATLAB. The result of the kinetic energies as a function of intensity from 1×10^{14} to 4×10^{14}W/cm^2 were shown in Figure 30. For H^+, kinetic energy

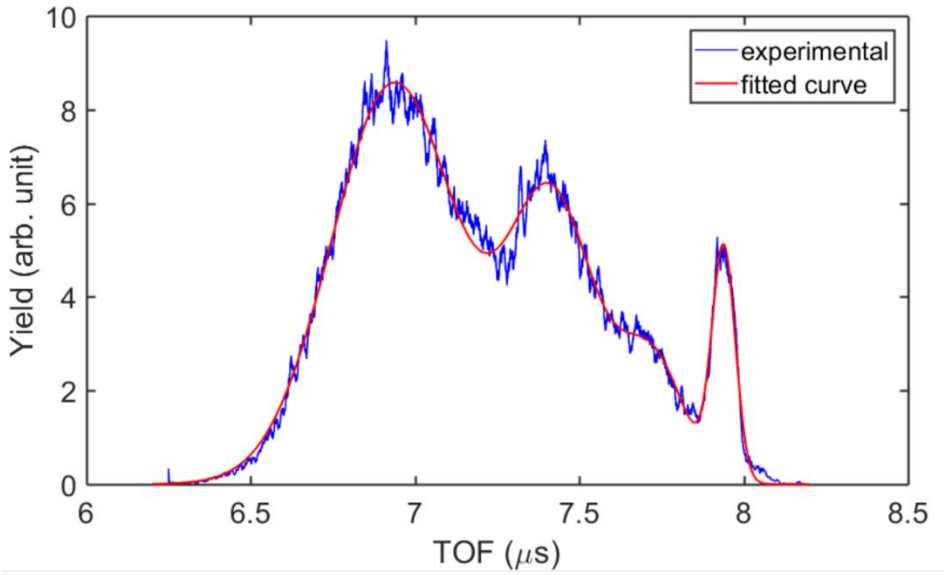

Figure 29. TOF of H^+ ejected from ethane obtained with linear TOFMS (blue) and Gaussian were fitted to the H^+ peaks (red).

of the first peak is increasing with the increasing intensity from 7eV to 13eV. This peak has similar trend with the H^+ ejected from acetonitrile that were attributed to Coulomb explosion. Therefore, we can conclude that this broad peak is also originated via Coulomb explosion. The other peaks in the spectra have similar kinetic energies within all the intensity range. For H_2^+, kinetic energies of all three peaks are not changing explicitly. First peak has the kinetic energies around 2.5eV, second peak has the kinetic energies

around 1.2eV and third peak has the kinetic energies of around 0.2eV within all the intensity ranges. Lastly, H_3^+ peak also does not show significant intensity dependence. The kinetic energy of this peak changes from 0.20 eV to 0.24 eV.

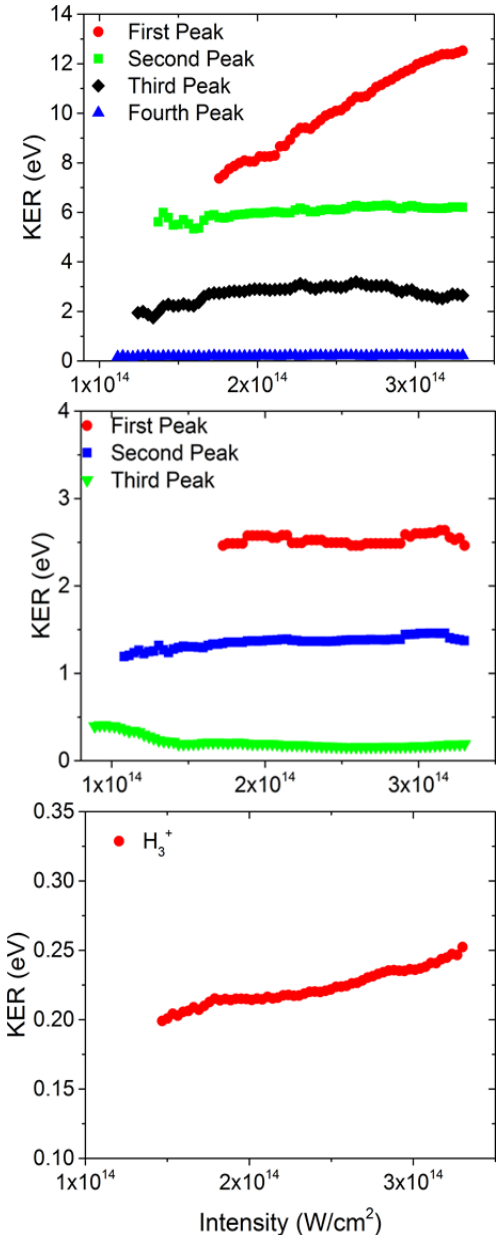

Figure 30. Kinetic energies of atomic (upper panel), diatomic (middle panel) and triatomic (lower panel) hydrogen as a function of intensity.

6.4 Conclusions

The interaction of the hydrocarbon molecule ethane with an intense fs laser pulses was experimentally studied with a linear TOFMS. The products H^+, H_2^+ and H_3^+ were the main focus in this work. Total four peaks and three peaks were found to exist for atomic and diatomic hydrogen ions, while only one peak were found to exist for triatomic hydrogen ion. Angular distributions of these ionic hydrogen species exhibit different behaviors for each peak. Intensity dependences showed that the peak arriving earliest in time was originated at higher intensities. Kinetic energies were measured as function of intensity, and it was found that the broad peak that comes earlier in the TOF spectrum of H^+ was due to Coulomb explosion.

CHAPTER VII

PHOTO-ELECTRON ENERGY SPECTRUM AND ANGULAR DISTRIBUTIONS OF THE SODIUM ATOM

7.1 Introduction

Studies of alkali atoms in multiphoton ionization region provide precious data for better understanding of the interaction of intense laser light and matter. Since they only have one valance electron on the most outer shell, the ionization energies are small. Therefore, photoionization occurs through absorption of only a few photons which attracts scientists for the investigation of MPI process. Another advantage of alkali metals is simplicity of the energy level scheme which makes easy to understand and interpret the results. One of the common tools to study MPI studies is measuring the photoelectron angular distributions (PAD) which gives precious insight into the atomic transitions. The angular distributions of electrons can vary depending on the initial and intermediate states and final continuum state involved in the process. Most of the experiment on PADs have been done using Xe and hydrogen atoms so far [16, 60, 61], but studies with alkali atoms are very rare. Especially, experimental and theoretical investigations on sodium atom is very scarce.

If ionization occurs with a single photon, the photoelectron angular distributions are given by the general expression:

$$\frac{d\sigma}{d\Omega} = \frac{\sigma}{4\pi}\left(1+\beta_2 P_2\left(\cos\theta\right)\right) \tag{7.1}$$

where $d\sigma/d\Omega$ is the differential cross section, σ is the integrated cross section, Ω is the solid angle, $P_n(\cos\theta)$ is the Legendre polynomial of order n. β is the anisotropy or asymmetry parameter which has values between -1 and 2 [62, 63]. In multiphoton ionization case, the angular distributions of photoelectron can be determined by the higher order Legendre polynomials. For example, for n-photon ionization, angular distributions can be determined with:

$$\frac{d\sigma}{d\Omega} = \frac{\sigma}{4\pi}\left(\sum_{i=0}^{n} \beta_{2i} P_{2i}\left(\cos\theta\right)\right) \tag{7.2}$$

7.2 Energy levels of the sodium atom

Sodium is a chemical element having the atomic symbol Na and it is classified as an alkali metal. It is light and silver colored appearance. Its atomic number is 11 and atomic mass is 22.9898 ($^{23}_{11}\mathrm{Na}$). It has a single electron in its most outer shell, so that electron can be removed easily. At room temperature and atmospheric pressure, it exists as a solid, but it is soft metal that can be easily cut. The melting point of Na is 207.9 °F (97.72 °C) and boiling point is 1621 °F (883 °C).

The excitation and ionization pathways of sodium atoms when interacted with 800nm and 50fs laser pulses is depicted in Figure 31. This information was obtained from the NIST (National Institute of Standards and Technology) webpage. With the specified laser parameters, different excitation pathways to reach the continuum are possible. The most dominant pathway is a 2+1+1 resonant enhanced multiphoton ionization (REMPI)

process through a transition from 3s to 4s state by absorption of two photons (red arrows in Figure 31). After the 4s state is populated, population goes to the 5p, 6p and 7p states after absorption of a photon. From there the absorption of a fourth photon, gives rise to photo-electrons by reaching the ionization continuum. Energy levels describing this are shown in Table 4.

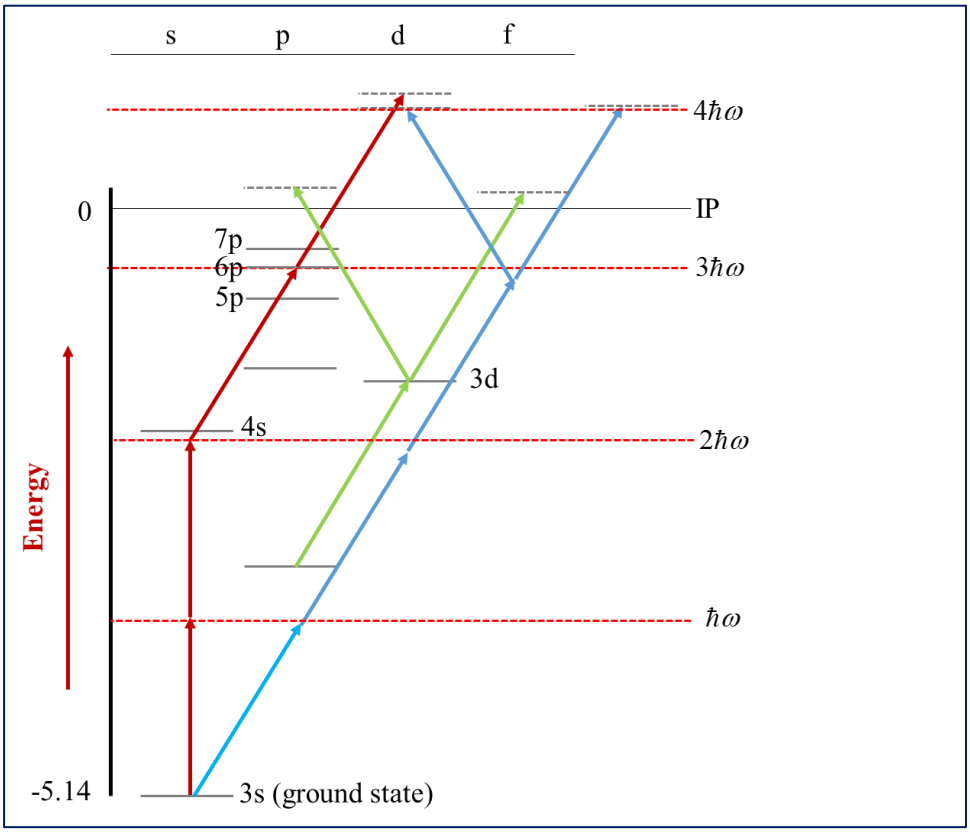

Figure 31. Multiphoton excitation pathways of sodium atom when interacted with 800 nm laser pulses. Right axis shows the energy in photon unit, while left axis displays the energy in unit of eV. Each arrow having different colors presents one photon energy. Red arrows show the most dominant excitation pathway to continuum.

Table 4. Energy levels of sodium atom that are used in this research. Left column (n) shows the principle quantum numbers, while column s, p, d present the angular momentum of each state.

n	s	p	d
7		-0.36eV	
6		-0.51eV	
5		-0.79eV	
4	-1.95eV		
3	-5.14eV		-1.52eV

7.3 Experimental details

We performed our experiments on sodium atom using the ATI apparatus which was described in detail in chapter 3. We also used the same laser system that has been used in previous experiments. ATI apparatus was pump down to the base pressure of $\sim 10^{-8}$ mbar. Then, the oven turned on to heat and evaporate the sodium atoms. Sodium was diffused through a hole, which has the diameter of 0.25mm, from the oven into the chamber. Laser radiation was focused to the center of the vacuum chamber using a 20 cm achromatic lens. The oven was moved around using a translational stage to get maximum integrated electron yield on TOF spectrum. A half wave plate was placed into the laser beam path before the chamber window to rotate the polarization angle. Polarization angle was controlled in automated fashion using the LabVIEW program. Polarization angle is rotated from 0° to 90° with increment of 1°. We measured angular distributions at two different laser intensities. The ejected electrons travel inside the field-free μ-metal and then are detected at the MCP. Electron TOFs for each angle were recorded using the same FAST

ComTec MCS6 multiple-event time digitizer. The same pre-amplifier, Mini Circuit ZKL-2, was inserted between MCP and MCS6 box to amplify the signal from MCP and to protect the MCS6 box in case large signals are produced by MCP.

7.4 Energy spectrum of sodium atom

Another important method to understand the MPI process can be achieved by measuring energy-resolved photoelectrons. Ejected electron might absorb more photons than minimum required number of photon for ionization, which is known as ATI. The feature of ATI peaks is that it consists of several peaks that are separated by one photon energy (in our case one photon energy is 1.55eV). The recorded electron TOF spectrum can be converted into energy spectrum. The counter records the time that takes for an electron to travel from ionization region to the MCP. Then TOF can be converted using the simple kinetic energy equation:

$$E = \frac{1}{2} m_e v^2 = \frac{1}{2} m_e \left(\frac{L}{t + \delta t} \right)^2 \tag{7.3}$$

where m_e the electron is mass, L is the distance between ionization region and MCP, t is measured time, and δt is time delay. L and δt are free parameters that need to be adjusted in order to present the ATI spectrum properly. L is adjusted such that the energy difference between each ATI peak is equal to 1 photon energy (1.55eV), and δt is adjusted such that the peaks on the energy spectra are positioned correctly. In our experiments, we set $L = 0.40m$ and $\delta t = -3.9ns$.

An example of conversion from TOF spectrum to energy spectrum is depicted in Figure 32. Zero order ATI peak for 5p state has an energy of ~0.8eV, while first order ATI

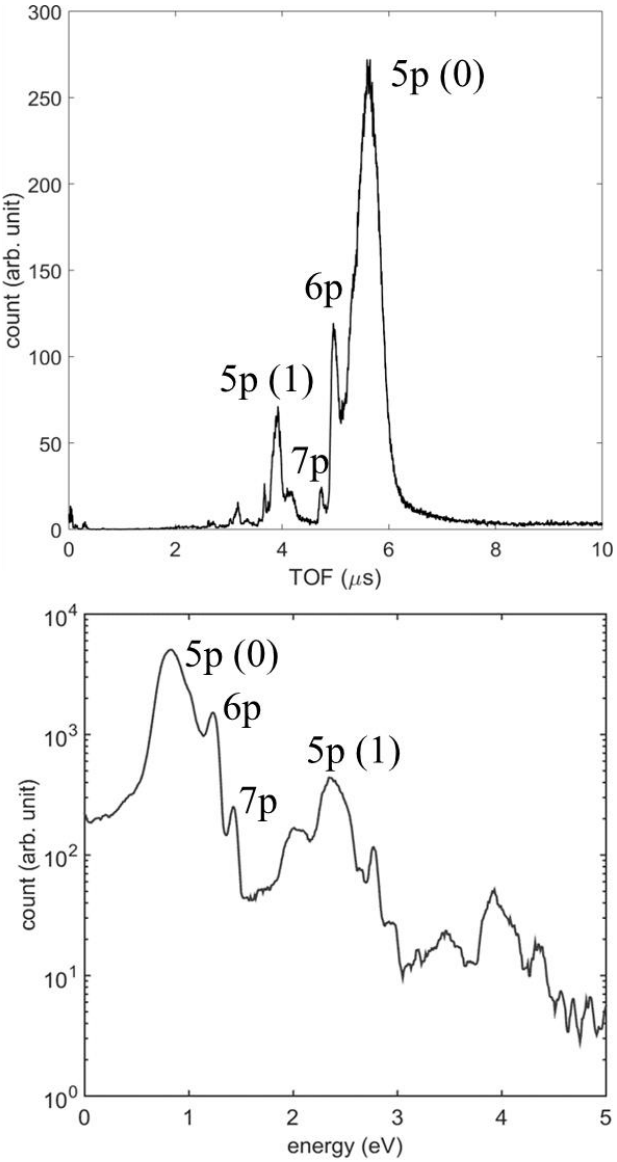

Figure 32. Upper panel shows the TOF spectrum of electron yields, while lower panel presents typical ATI energy spectrum of sodium atom. The data in upper panel was converted to kinetic energy and presented in a semi-log plot in lower panel. The ionizations from 5p, 6p, and 7p states are observed.

peak has an energy of ~2.35eV. As it is expected, ATI peaks are separated by one photon energy which is 1.55eV.

7.5 Photoelectron angular distributions (PADs) from ATI of sodium

In this part, we discuss experimental measurements of PADs resulting from the ionization of atomic sodium. Linear laser radiation was used so that the sodium atom is ionized through the absorption of 4 photons. By using two different laser intensity, dependence of PADs on laser intensity were also studied. Neutral density filter was used to attenuate the laser power. The ATI energy spectrum at the intensity of $2\times10^{13}\mathrm{W/cm^2}$ is shown in Figure 33. ATI peaks for 5p states up to three order were observed, so that PADs of these ATI

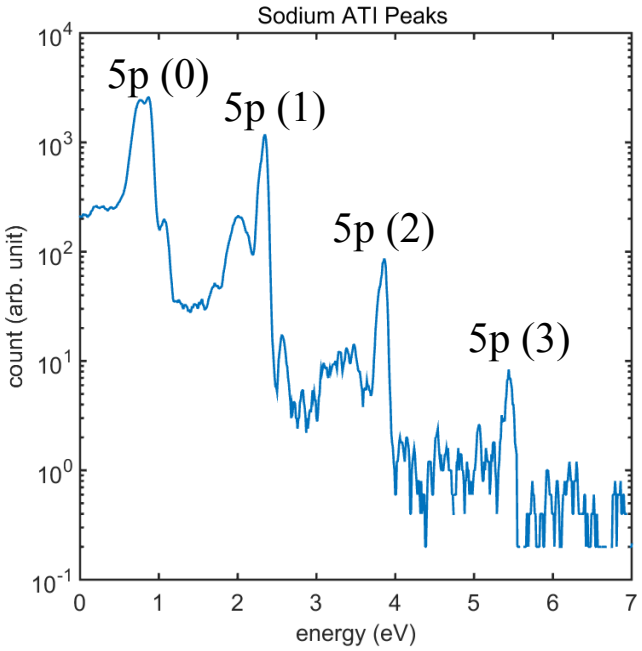

Figure 33. Energy spectrum of sodium atom showing the ATI peaks from zero order to third order for state 5p. Angular distributions have been determined using this energy spectrum for each ATI peak.

peaks were our main focus in this study. PADs in MPI region are depend on the number of photons involved and initial and intermediate levels which photoelectron is ejected. We

consider that electrons are produced through the process $3s \rightarrow\rightarrow 4s \rightarrow 5p \rightarrow e^-$. Here, each arrow indicate the number of photons involved for each step.

Figure 34 shows experimental PADs from 5p states for zero, first, second and third order ATI peaks at the intensity of $2\times10^{13}\text{W/cm}^2$. The squares represent the experimental data points, which were measured from 0° to 90° and reflected to 90° to 180° for better viewing. Solid lines show the least squared fits of the measured angular distributions to the Eq. (7.2). Since zero order ATI requires at least four photons, the best fit was obtained using the Eq. (7.2) including up to 8 order, i.e $\frac{d\sigma}{d\Omega} = \frac{\sigma}{4\pi}\left(1+\beta_2 P_2\left(\cos\theta\right)+\beta_4 P_4\left(\cos\theta\right)+\beta_6 P_6\left(\cos\theta\right)+\beta_8 P_8\left(\cos\theta\right)\right)$. Similarly, our data fits well for the first order ATI peak when the Eq. (7.2) expanded up to 10 order. For the

Table 5. σ and β fitting parameters for each angular distribution of ATI peaks at the intensity of $2\times10^{13}\text{W/cm}^2$ to $d\sigma/d\Omega = (\sigma/4\pi)(\sum_{i=0}^{n}\beta_{2i}P_{2i}(\cos\theta))$.

	σ	β_2	β_4	β_6	β_8	β_{10}	β_{12}	β_{14}
5p(0)	0.1588	0.3638	0.2663	0.1831	-0.0894	_	_	_
5p(1)	0.1329	0.3138	0.1542	0.1883	0.1871	-0.0794	_	_
5p(2)	0.1792	0.3325	-0.0160	0.0779	0.2139	0.1614	0.0214	_
5p(3)	0.1828	0.3154	-0.0904	0.0039	0.1868	0.1783	0.1508	-0.0038

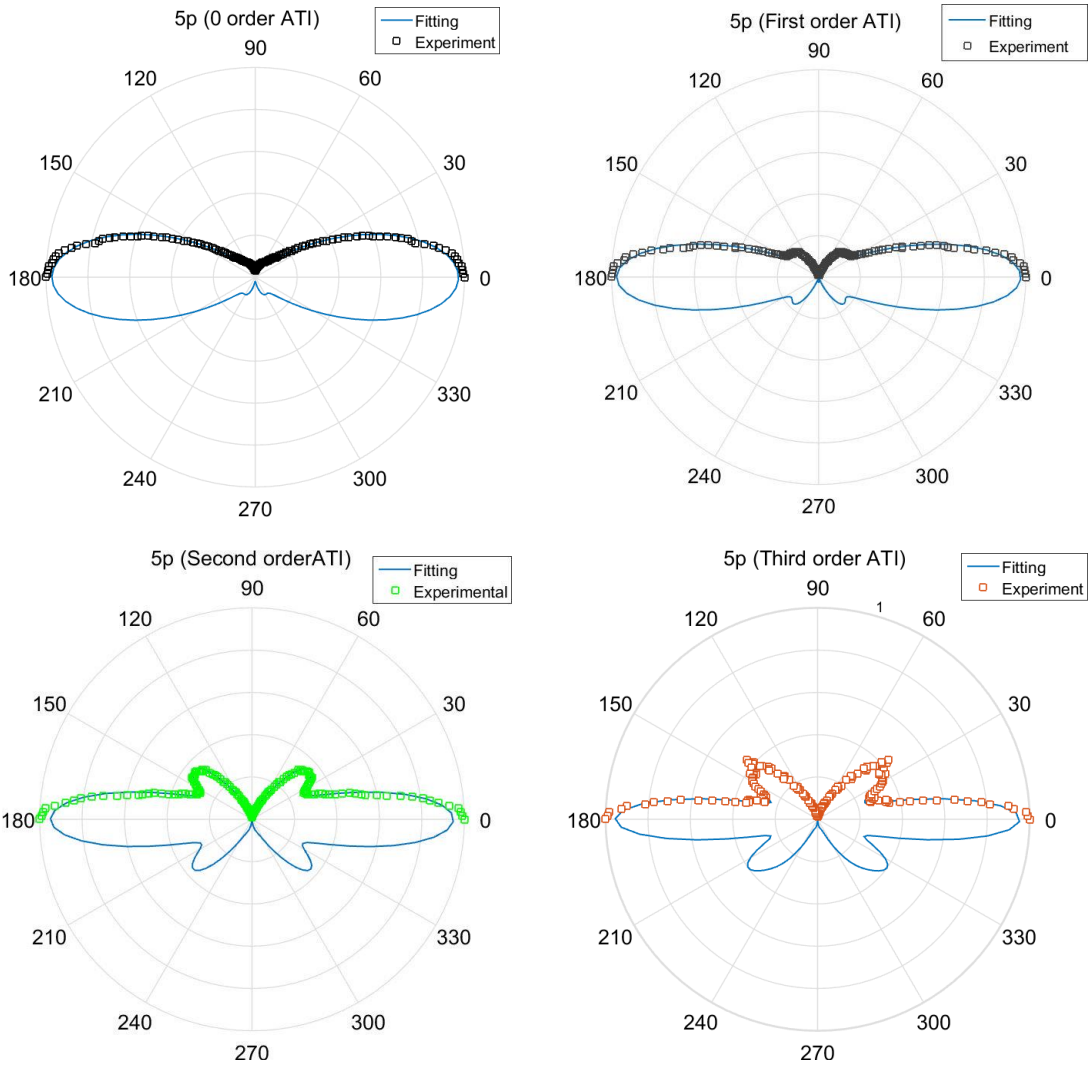

Figure 34. Photo-electron angular distributions of sodium atom at the intensity of $2\times10^{13}\mathrm{W/cm}^2$. Upper panel shows angular distributions of zero and first order ATI while lower panel shows angular distribution of the second and third order ATI through 5p state. Squares show experimental data and solid lines show fitting curves.

second order and third order ATI peaks, the Eq. (7.2) was expanded up to 12 and 14 order as well. Experimental fitting parameters for each ATI peak are shown in Table 5. For the zero order ATI peak, where the minimum number of photon absorbed, angular distribution shows anisotropic behavior having maximum at 0° and 180° and minimum at 90° and there is a small side lobe at ~60°. For the first, second and third ATI peaks, angular distributions present similar structure as zero order ATI peak, but with the increasing ATI order the lobes are getting more pronounced. We also observed that with the increasing ATI order, the position of the maximum electron yield on the side lobes are shifting. For example; for the zero order ATI peak, maximum electron yield on the side lobe at around 60° while for the third order ATI maximum electron yield is observed around 30°. Another feature of angular distributions is that width of the angular distribution is becoming smaller with the increasing ATI order.

In Figure 35 angular distribution of the zero, first and second order ATI from 5p state at the intensity of $1\times10^{13}\text{W/cm}^2$ and $2\times10^{13}\text{W/cm}^2$ are compared. Third order ATI peak is not strong enough for analyzing, so that third order ATI peak is excluded. As can be seen from the Figure 35, intensity does not play a significant role on photo-electron angular distributions. The number of side lobes are the same, but the shape of the side lobes slightly different for different intensities. This is most probably due to high ionization rate at higher intensity.

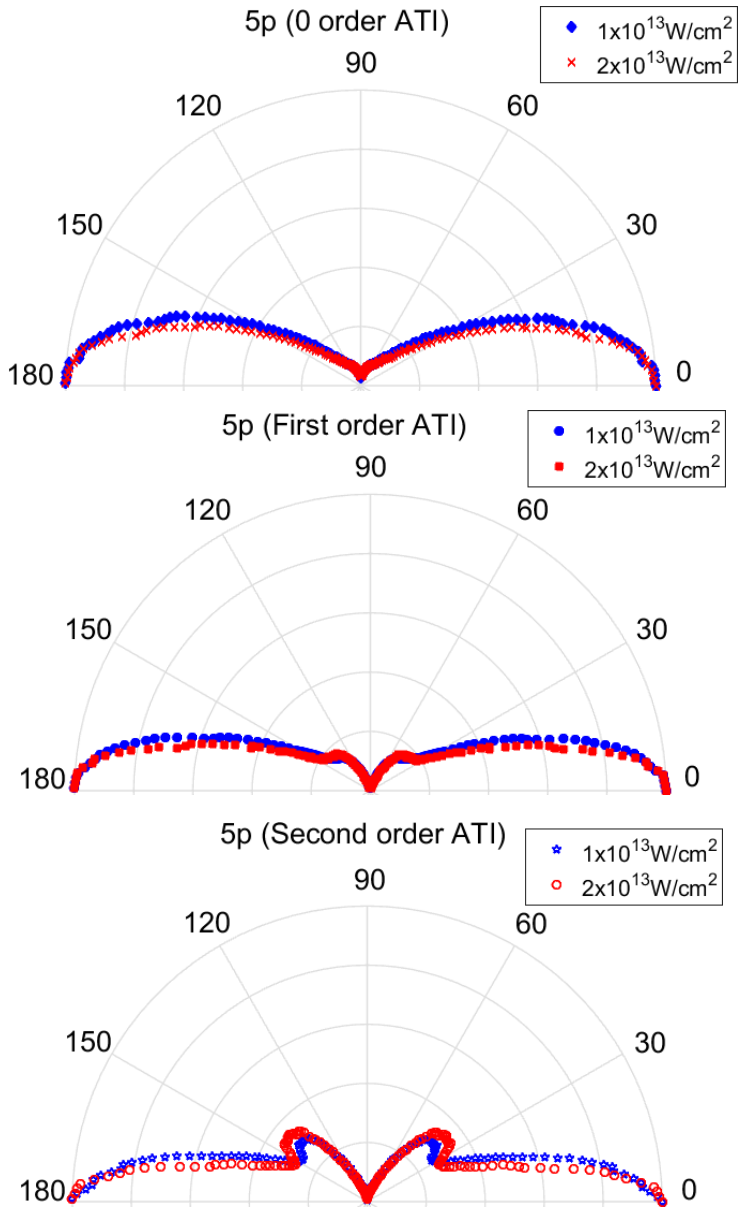

Figure 35. Comparison of the angular distributions of the zero, first, and second order ATI peaks through 5p state at the intensity of 2×10^{13}W/cm^2 (red) and 1×10^{13}W/cm^2 (blue).

7.6 Conclusions

In this chapter, we have shown experimental results for four-photon ionization of sodium atoms in the near infrared spectral region. TOF of electrons were measured using the ATI apparatus. Kinetic energies of the photo-electrons were determined by converting the TOF spectrum to the kinetic energy spectrum. Intermediate levels 5p, 6p and 7p were identified in the energy spectrum by following up the results from the NIST. Angular distributions of the photo-electrons ionized via the 5p state were investigated for the ATI order of up to three. A general expression given for the photo-electron angular distributions were used to fit the experimental data. Agreement between the experimental data and fitting functions were satisfactory for the ionization through 5p states. Angular distributions present anisotropic behavior having maxima at 0 degree and minima at 90 degrees. There are also side lobes existing between 60 and 30 degrees depending on the ATI order. We observed that the maximum point of the side lobes is shifting to smaller angles with the increasing ATI order. Another remark is that the side lobes are more pronounced for higher order ATI peaks. Finally, we concluded that angular distributions of the photo-electrons are not depend on the laser polarization significantly, as we observed no major difference on the angular distributions at two different intensities.

CHAPTER VIII

SUMMARY AND GENERAL CONCLUSIONS

In this dissertation, the ionization and dissociation of polyatomic molecules CH_3CN and C_2H_6 exposed to an intense fs laser pulses were experimentally investigated using a TOFMS. These experiments include the intensity and angular dependences of the parent ion CH_3CN^+ and other smaller fragments by operating the TOFMS in reflectron mode. For angular dependences, lighter fragment ions present anisotropic behavior, while heavier fragment ions were not affected much when polarization direction was changed from 0 to 360 degree. Intensity dependences were investigated between the intensities of 4.4×10^{13} and $3.3\times10^{14}W/cm^2$. The result of the power dependences showed that the parent molecules were excited by a multiphoton process which leads to dissociation of molecules into smaller fragments in the excited state. Appearance energy of the fragment ions were calculated with the quantum chemistry code GAMESS, and the results were consistent with the experimental results. Next, kinetic energy measurements, intensity dependences and angular distributions of the H^+ ion formed through the dissociation of CH_3CN was also studied in linear mode operation of TOFMS. Different mechanisms such as Coulomb explosion, FAD, and QET were involved in the dissociation and ionization of the H^+ ions.

Furthermore, formation of H^+, H_2^+, and H_3^+ from ethane were studied experimentally using the linear TOFMS. The dependence of the ionization yields on the laser intensity and laser polarization on the formation of these hydrogen species were investigated. H^+ ion from ethane exhibits different structure than H^+ ion from acetonitrile.

We observed three different peaks for the formation of H^+ from acetonitrile, while four different mechanisms were observed for the formation of H^+ from ethane. Three peaks and only one peak were responsible for the formation of the H_2^+ and H_3^+ ions. Each peak of the hydrogen ion species behave differently when polarization direction was varied. As a result of intensity dependences, we concluded that the first peak in TOF spectrum of H^+ was occurred via Coulomb explosion.

Finally, photo-electron kinetic energy and angular distributions of sodium atom were measured with the ATI apparatus. Zero order ATI peaks for 5p, 6p and 7p states as well as first, second and third ATI peaks for 5p states were existed in the energy spectrum. Angular distributions of photo-electrons ejected from 5p states were measured for different ATI orders. It was found that a lobe appears at around 60 degrees. With the increasing ATI order, the lobe is getting more pronounced and maximum value of the lobe is shifting from 60 degree to 40 degree. The structure of the angular distributions were found to not depend on the laser intensity since their structure are similar at two different intensity.

This study opens the way for different works for future consideration. For instance, dissociation of methyl isonitrile (CH_3NC) that is isomeric to acetonitrile could be studied to see, for example, if N atom will produce perpendicular fragmentation. Furthermore, the dissociation and ionization dynamics of the acetonitrile molecule can be controlled by aligning the parent molecule using a pump and a probe pulse having an appropriate time delay. Besides, for future experiments more molecules could be added to the comparison of H^+ ion formation.

REFERENCES

[1] N.A. Papadogiannis, B. Witzel, C. Kalpouzos, D. Charalambidis, Observation of Attosecond Light Localization in Higher Order Harmonic Generation, Physical Review Letters 83 (1999) 4289-4292.

[2] M. Hentschel, R. Kienberger, C. Spielmann, G.A. Reider, N. Milosevic, T. Brabec, P. Corkum, U. Heinzmann, M. Drescher, F. Krausz, Attosecond metrology, Nature 414 (2001) 509-513.

[3] J.H. Posthumus, The dynamics of small molecules in intense laser fields, Reports on Progress in Physics 67 (2004) 623.

[4] J.E. Bayfield, P.M. Koch, Multiphoton Ionization of Highly Excited Hydrogen Atoms, Physical Review Letters 33 (1974) 258-261.

[5] R.P. Singhal, H.S. Kilic, K.W.D. Ledingham, C. Kosmidis, T. McCanny, A.J. Langley, W. Shaikh, Multiphoton ionisation and dissociation of NO_2 by 50 fs laser pulses, Chemical Physics Letters 253 (1996) 81-86.

[6] P. Agostini, F. Fabre, G. Mainfray, G. Petite, N.K. Rahman, Free-Free Transitions Following Six-Photon Ionization of Xenon Atoms, Physical Review Letters 42 (1979) 1127-1130.

[7] D.B. Milošević, G.G. Paulus, D. Bauer, W. Becker, Above-threshold ionization by few-cycle pulses, Journal of Physics B: Atomic, Molecular and Optical Physics 39 (2006) R203.

[8] N.A. Hart, J. Strohaber, A.A. Kolomenskii, G.G. Paulus, D. Bauer, H.A. Schuessler, Selective strong-field enhancement and suppression of ionization with short laser pulses, Physical Review A 93 (2016) 063426.

[9] L.V. Keldysh, Ionization in the field of a strong electromagnetic wave, Soviet Physics JETP 20 (1965) 1307-1314.

[10] J. Strohaber, F. Zhu, A.A. Kolomenskii, H.A. Schuessler, Observation of anisotropic fragmentation in methane subjected to femtosecond radiation, Physical Review A 89 (2014) 023430.

[11] S. Wang, X. Tang, L. Gao, M.E. Elshakre, F. Kong, Dissociation of Methane in Intense Laser Fields, The Journal of Physical Chemistry A 107 (2003) 6123-6129.

[12] X.-p. Tang, S.-f. Wang, M.E. Elshakre, L.-r. Gao, Y.-l. Wang, H.-f. Wang, F.-a. Kong, The Field-Assisted Stepwise Dissociation of Acetone in an Intense Femtosecond Laser Field, The Journal of Physical Chemistry A 107 (2003) 13-18.

[13] E. Baldit, S. Saugout, C. Cornaggia, Coulomb explosion of N_2 using intense 10- and 40-fs laser pulses, Physical Review A 71 (2005) 021403.

[14] C. Jianxin, M. Ri, L. Xia, R. Haizhen, Y. Hong, G. Qihuang, Coulomb explosion of propane in intense femtosecond laser fields, Journal of Physics B: Atomic, Molecular and Optical Physics 37 (2004) 2501.

[15] R.N. Compton, J.A.D. Stockdale, C.D. Cooper, X. Tang, P. Lambropoulos, Photoelectron angular distributions from multiphoton ionization of cesium atoms, Physical Review A 30 (1984) 1766-1774.

[16] M. Li, Y. Liu, H. Liu, Y. Yang, J. Yuan, X. Liu, Y. Deng, C. Wu, Q. Gong, Photoelectron angular distributions of low-order above-threshold ionization of Xe in the multiphoton regime, Physical Review A 85 (2012) 013414.

[17] C. Cornaggia, P. Hering, Nonsequential double ionization of small molecules induced by a femtosecond laser field, Physical Review A 62 (2000) 023403.

[18] M. Schuricke, G. Zhu, J. Steinmann, K. Simeonidis, I. Ivanov, A. Kheifets, A.N. Grum-Grzhimailo, K. Bartschat, A. Dorn, J. Ullrich, Strong-field ionization of lithium, Physical Review A 83 (2011) 023413.

[19] R.R. Freeman, P.H. Bucksbaum, H. Milchberg, S. Darack, D. Schumacher, M.E. Geusic, Above-threshold ionization with subpicosecond laser pulses, Physical Review Letters 59 (1987) 1092-1095.

[20] P.W. Harland, B.J. McIntosh, Enthalpies of formation for the isomeric ions H_xCCN^+ and H_xCNC^+ (x = 0−3) by "monochromatic" electron impact on C_2N_2, CH_3CN and CH_3NC, International Journal of Mass Spectrometry and Ion Processes 67 (1985) 29-46.

[21] J.L. Franklin, Y. Wada, P. Natalis, P.M. Hierl, Ion-Molecule Reactions in Acetonitrile and Propionitrile1a, The Journal of Physical Chemistry 70 (1966) 2353-2361.

[22] C. Wu, Y. Xiong, Z. Gao, F.a. Kong, H. Lu, X. Yang, Z. Xu, Ionization and dissociation of acetonitrile by intense femtosecond laser pulse, Chin.Sci.Bull. 45 (2000) 1953-1955.

[23] J. Strohaber, Intense-Field Ionization Of Atoms And Molecules: Spatially Resolved Ion Detection And Ultrashort Optical Vortices, Physics and Astronomy, University of Nebraska, 2008.

[24] P.H. Bucksbaum, A. Zavriyev, H.G. Muller, D.W. Schumacher, Softening of the H_2^+ molecular bond in intense laser fields, Physical Review Letters 64 (1990) 1883-1886.

[25] L.J. Frasinski, J.H. Posthumus, J. Plumridge, K. Codling, P.F. Taday, A.J. Langley, Manipulation of Bond Hardening in H_2^+ by Chirping of Intense Femtosecond Laser Pulses, Physical Review Letters 83 (1999) 3625-3628.

[26] P. Maine, D. Strickland, P. Bado, M. Pessot, G. Mourou, Generation of ultrahigh peak power pulses by chirped pulse amplification, IEEE Journal of Quantum Electronics 24 (1988) 398-403.

[27] V.I.K. B.A. Mamyrin, D.V. Shmikk, V.A. Zagulin, The mass-reflectron, a new nonmagnetic time-of-flight mass spectrometer with high resolution, Journal of Experimental and Theoretical Physics 37 (1973) 82.

[28] F.A. Rajgara, M. Krishnamurthy, D. Mathur, Electron rescattering and the dissociative ionization of alcohols in intense laser light, The Journal of Chemical Physics 119 (2003) 12224-12230.

[29] C. Cornaggia, M. Schmidt, D. Normand, Coulomb explosion of CO_2 in an intense femtosecond laser field, Journal of Physics B: Atomic, Molecular and Optical Physics 27 (1994) L123.

[30] F.A. Ilkov, T.D.G. Walsh, S. Turgeon, S.L. Chin, Dissociative tunnel ionization of H_2 in an intense mid-ir laser field, Physical Review A 51 (1995) R2695-R2698.

[31] A. Giusti-Suzor, F.H. Mies, L.F. DiMauro, E. Charron, B. Yang, Dynamics of H_2^+ in intense laser fields, Journal of Physics B: Atomic, Molecular and Optical Physics 28 (1995) 309.

[32] C. Tian, C.R. Vidal, Electron impact dissociative ionization of ethane: Cross sections, appearance potentials, and dissociation pathways, The Journal of Chemical Physics 109 (1998) 1704-1712.

[33] M. Oppermann, S.J. Weber, F. Morales, M. Richter, S. Patchkovskii, A. Csehi, V. Á, M. Ivanov, O. Smirnova, J.P. Marangos, Control and identification of strong field dissociative channels in CO_2 via molecular alignment, Journal of Physics B: Atomic, Molecular and Optical Physics 47 (2014) 124025.

[34] J. McKenna, M. Suresh, B. Srigengan, I.D. Williams, W.A. Bryan, E.M.L. English, S.L. Stebbings, W.R. Newell, I.C.E. Turcu, J.M. Smith, E.J. Divall, C.J. Hooker, A.J. Langley, J.L. Collier, Ultrafast ionization study of N_2 in intense linearly and circularly polarized laser fields, Physical Review A 73 (2006) 043401.

[35] D.Y. Sorokin, S. van Pelt, T.P. Tourova, S. Takaichi, G. Muyzer, Acetonitrile degradation under haloalkaline conditions by Natronocella acetinitrilica gen. nov., sp. nov, Microbiology 153 (2007) 1157-1164.

[36] C. Mui, M.A. Filler, S.F. Bent, C.B. Musgrave, Reactions of Nitriles at Semiconductor Surfaces, The Journal of Physical Chemistry B 107 (2003) 12256-12267.

[37] V. Wakelam, I.W.M. Smith, E. Herbst, J. Troe, W. Geppert, H. Linnartz, K. Öberg, E. Roueff, M. Agúndez, P. Pernot, H.M. Cuppen, J.C. Loison, D. Talbi, Reaction Networks for Interstellar Chemical Modelling: Improvements and Challenges, Space Science Reviews 156 (2010) 13-72.

[38] A.H. Delsemme, Pristine nature of comets as revealed by their UV spectrum, Appl. Opt. 19 (1980) 4007-4014.

[39] O. Nešković, M. Veljković, D.a. Golobоćanin, M. Miletić, K.F. Zmbov, Electron impact study of the appearance energies of positive ions from CH_3CN, International Journal of Mass Spectrometry and Ion Physics 44 (1982) 61-80.

[40] R.F. Lake, H. Thompson, The Photoelectron Spectra of Some Molecules Containing the C-N Group, Proceedings of the Royal Society of London. Series A, Mathematical and Physical Sciences 317 (1970) 187-198.

[41] R.H. Staley, J.E. Kleckner, J.L. Beauchamp, Relationship between orbital ionization energies and molecular properties. Proton affinities and photoelectron spectra of nitriles, Journal of the American Chemical Society 98 (1976) 2081-2085.

[42] R. Locht, J. Schopman, H. Wankenne, J. Momigny, The dissociative ionization of nitrogen, Chemical Physics 7 (1975) 393-404.

[43] P. Graham, K.W.D. Ledingham, R.P. Singhal, T. McCanny, S.M. Hankin, X. Fang, P. Tzallas, C. Kosmidis, P.F. Taday, A.J. Langley, The angular distributions of fragment ions from labelled and unlabelled N_2O in intense laser fields, Journal of Physics B: Atomic, Molecular and Optical Physics 33 (2000) 3779.

[44] S. Roither, X. Xie, D. Kartashov, L. Zhang, M.S. Schöffler, H. Xu, A. Iwasaki, T. Okino, K. Yamanouchi, A. Baltuska, M. Kitzler, High energy proton ejection from hydrocarbon molecules driven by highly efficient field ionization, Journal of Physics: Conference Series 388 (2012) 032063.

[45] E. Sonia, L.C. Cody, R. Arthur, L. Erik, L. Seyedreza, H. Václav, B. Sergiy, K. Markus, G. Stefanie, B. Andrius, X. Xinhua, Y. Kaoru, V. Kálmán, K. Markus, Enhanced ionisation of polyatomic molecules in intense laser pulses is due to energy upshift and field coupling of multiple orbitals, Journal of Physics B: Atomic, Molecular and Optical Physics 50 (2017) 125601.

[46] S. Bubin, M. Atkinson, K. Varga, X. Xie, S. Roither, D. Kartashov, A. Baltuška, M. Kitzler, Strong laser-pulse-driven ionization and Coulomb explosion of hydrocarbon molecules, Physical Review A 86 (2012) 043407.

[47] L.J. Frasinski, K. Codling, P. Hatherly, J. Barr, I.N. Ross, W.T. Toner, Femtosecond dynamics of multielectron dissociative ionization by use of a picosecond laser, Physical Review Letters 58 (1987) 2424-2427.

[48] M.J.J. Vrakking, Control of the Coulomb explosion of I2, Eur. Phys. J. D 26 (2003) 111-118.

[49] O. Kornilov, M. Eckstein, M. Rosenblatt, C.P. Schulz, K. Motomura, A. Rouzée, J. Klei, L. Foucar, M. Siano, A. Lübcke, F. Schapper, P. Johnsson, D.M.P. Holland, T. Schlathölter, T. Marchenko, S. Düsterer, K. Ueda, M.J.J. Vrakking, L.J. Frasinski, Coulomb explosion of diatomic molecules in intense XUV fields mapped by partial covariance, Journal of Physics B: Atomic, Molecular and Optical Physics 46 (2013) 164028.

[50] X. Li, H.-Z. Ren, R. Ma, J.-X. Chen, H. Yang, Q.-H. Gong, The dissociative ionization and Coulomb explosion of ethane by a femtosecond laser field, Chinese Physics 13 (2004) 1564.

[51] P. Dietrich, P.B. Corkum, Ionization and dissociation of diatomic molecules in intense infrared laser fields, The Journal of Chemical Physics 97 (1992) 3187-3198.

[52] M. Thachuk, D.M. Wardlaw, Classical analysis of diatomic dissociation dynamics in intense laser fields, The Journal of Chemical Physics 102 (1995) 7462-7471.

[53] H.M. Rosenstock, M.B. Wallenstein, A.L. Wahrhaftig, H. Eyring, Absolute Rate Theory for Isolated Systems and the Mass Spectra of Polyatomic Molecules, Proceedings of the National Academy of Sciences of the United States of America 38 (1952) 667-678.

[54] T. Baer, P.M. Mayer, Statistical Rice-Ramsperger-Kassel-Marcus quasiequilibrium theory calculations in mass spectrometry, Journal of the American Society for Mass Spectrometry 8 (1997) 103-115.

[55] G. Wei, L. Xingqiang, Z. Dan, W. Xinlin, Pathway of H^+ in fragmentation of H_2 in 810 nm intense femtosecond laser fields, Physica Scripta 89 (2014) 025401.

[56] K. Hoshina, Y. Furukawa, T. Okino, K. Yamanouchi, Efficient ejection of H_3^+ from hydrocarbon molecules induced by ultrashort intense laser fields, The Journal of Chemical Physics 129 (2008) 104302.

[57] R. Itakura, J. Watanabe, A. Hishikawa, K. Yamanouchi, Ionization and fragmentation dynamics of benzene in intense laser fields by tandem mass spectroscopy, The Journal of Chemical Physics 114 (2001) 5598-5606.

[58] P.M. Kraus, M.C. Schwarzer, N. Schirmel, G. Urbasch, G. Frenking, K.-M. Weitzel, Unusual mechanism for H_3^+ formation from ethane as obtained by femtosecond laser pulse ionization and quantum chemical calculations, The Journal of Chemical Physics 134 (2011) 114302.

[59] K. Hoshina, H. Kawamura, M. Tsuge, M. Tamiya, M. Ishiguro, Metastable decomposition and hydrogen migration of ethane dication produced in an intense femtosecond near-infrared laser field, The Journal of Chemical Physics 134 (2011) 064324.

[60] M.J. Nandor, M.A. Walker, L.D.V. Woerkom, Angular distributions of high-intensity ATI and the onset of the plateau, Journal of Physics B: Atomic, Molecular and Optical Physics 31 (1998) 4617.

[61] L. Bai, J. Zhang, Z. Xu, D.-S. Guo, Photoelectron Angular Distributions from Above Threshold Ionization of Hydrogen Atoms in Strong Laser Fields, Physical Review Letters 97 (2006) 193002.

[62] Laboratory-Frame Photoelectron Angular Distributions in Anion Photodetachment: Insight into Electronic Structure and Intermolecular Interactions, Annual Review of Physical Chemistry 65 (2014) 341-363.

[63] K. Nakajima, T. Teramoto, H. Akagi, T. Fujikawa, T. Majima, S. Minemoto, K. Ogawa, H. Sakai, T. Togashi, K. Tono, S. Tsuru, K. Wada, M. Yabashi, A. Yagishita, Photoelectron diffraction from laser-aligned molecules with X-ray free-electron laser pulses, Scientific Reports 5 (2015) 14065.

APPENDIX A: TOFMS GENERAL DIAGRAM AND LABVIEW PROGRAMS

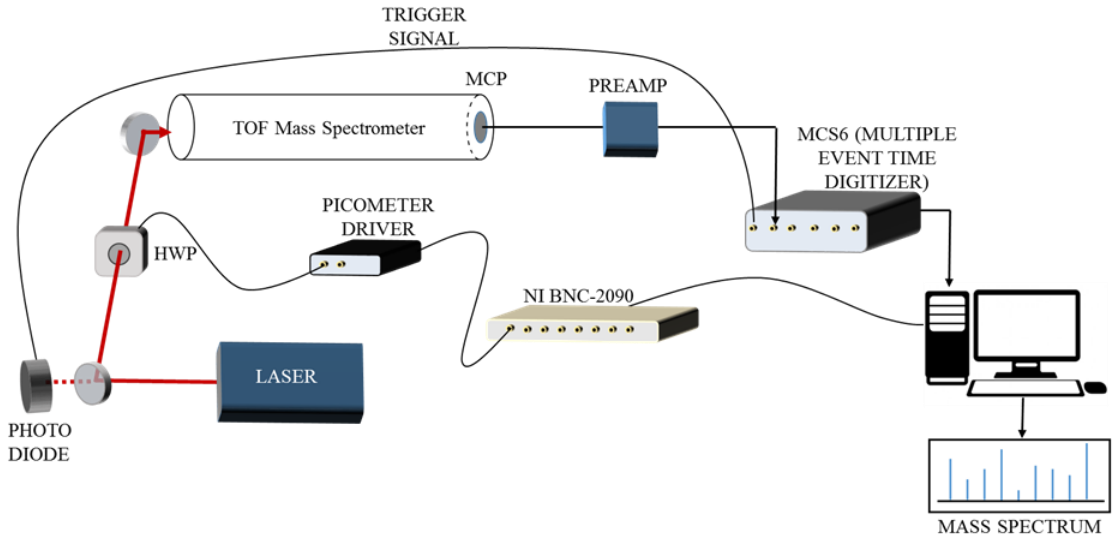

Figure 36. TOFMS general block diagram.

In figure 36 general diagram of TOFMS is shown. A photodiode is used to obtain trigger signal from the laser beam. The trigger signal is connected to the START channel of the MSC6 box. The signal from the MCP is connected to one of the STOP channels to record the data. When taking data with MCS6 box, we have a time resolution of 100ps. The sweep is started by a trigger (START) pulse. Then arrival time of ions relative to the trigger signal are recorded at STOP channels. Several operating mode can be selected to record the data. These are rising edge, falling edge and constant-fraction- timing (CFT). If falling/ rising edge is selected, the signal is counted when it goes from high to low/low to high transition. When different height signals are delivered from MCP, CFT mode can be used

to set a threshold level at constant fraction to each signal. A threshold value can be set between -1.5V and +1.5V. A pre-amplifier is inserted between MCP and MSC6 to amplify the signal from MCP. The pre-amplifier is also used to protect the MSC6 in case of a high voltage signal exceeding the threshold level of acquisition card is produced from MCP. The TOF data is recorded to the computer via MSC6 and this data can be converted to mass spectrum. A HWP is rotated with the picometer driver that is controlled by LabVIEW program. These LabVIEW programs can communicate with MCS6, so that each setting can be controlled from LabVIEW programs. In the following, LabVIEW programs that are used to control the laser polarization and intensity will be described in detail.

Front panel of LabVIEW program for rotational scan and pump probe experiments

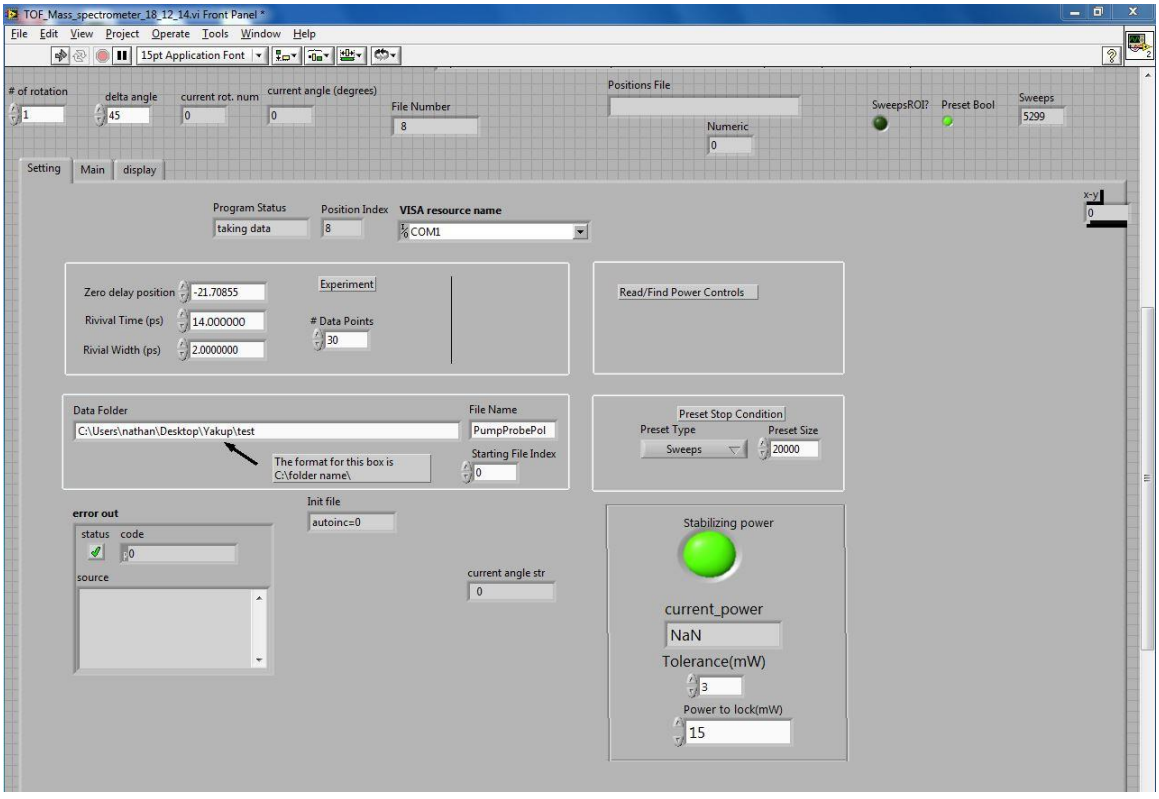

Delta angle: total rotation angle.

 # Of rotation: sets the number of steps to the delta angle. For example: If you would like to rotate the half wave plate by 90 degree with the increment of 2 degree set number of rotation to 45 and delta angle to 90.

Zero delay position: This part is used when pump probe experiments are performed. After you overlap the two beams, read the position of translational stage on the controller and type it in zero delay position.

Revival time: Set your molecule's revival time here in ps.

Revival width: Set range of your scan here. If revival time is 14ps and you set revival width as 2ps, then your scan will be between 13ps and 15ps.

#Data Points: Set the number of steps to scan your range.

Data folder: Copy and paste the folder name you would like to save your data.

File name: Name the files here. Your files will be saved with this name into your data folder.

Preset size: Set your integration time here. It is in unit of millisecond. If you want your integration time to be 1 minute for each step, set your preset size to 60000.

Front panel of LabVIEW program for intensity scans

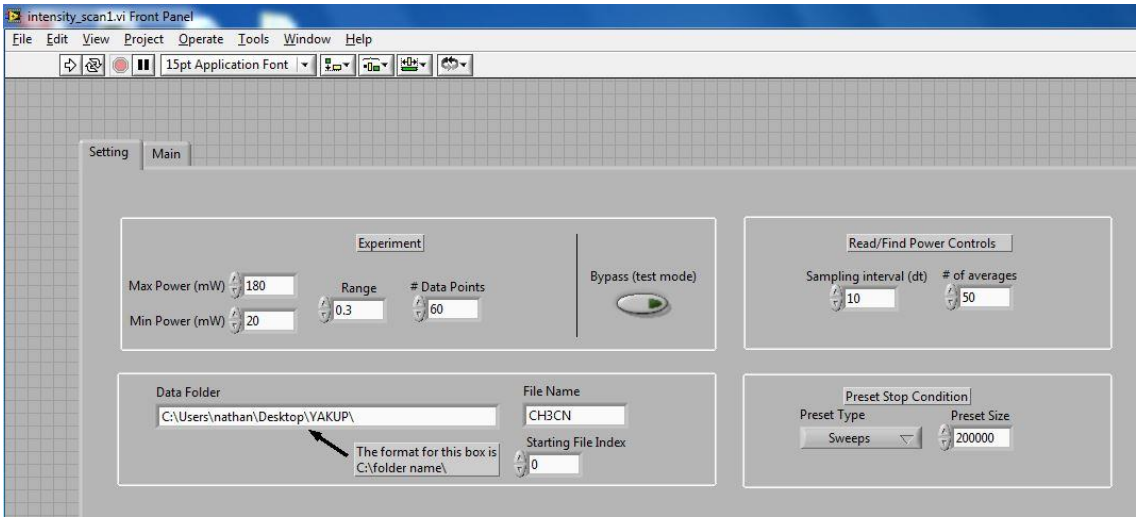

First, insert your power meter behind the chamber such that laser beam hits on power meter.

Max Power (mW): set your maximum power value that you would like to measure the ion yields or electron yields.

Min Power (mW): set your minimum power value that you would like to measure the ion yields or electron yields.

Range: the desired laser power will be set within this range. If your next power value is 30mw, and you set the range value as 0.3, your power will be set between 29.7 Mw and 30.3 Mw.

#Data Points: Set the number of steps between your minimum and maximum value.

Data folder: Copy and paste the folder name you would like to save your data.

File name: Name the files here. Your files will be saved with this name into your data folder.

MCS6 Setting Window

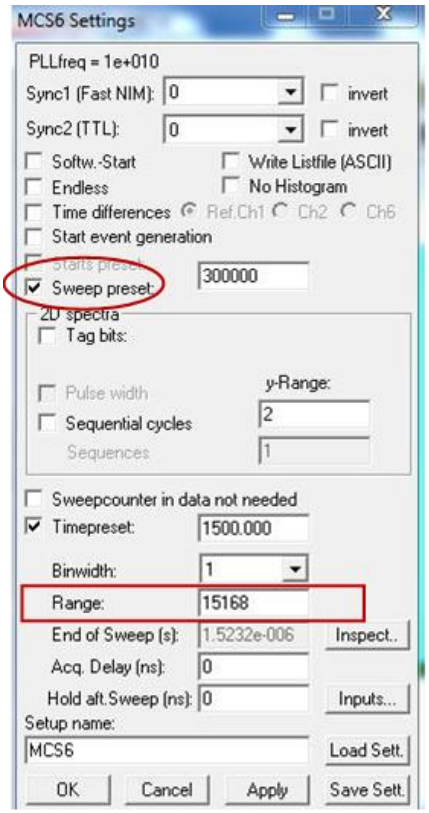

Set your TOF range here. The unit is 1/10 ns or 100 ps.

When LabVIEW programs are used, one needs to make sure that sweep preset on MCS6 settings should be clicked. You don’t need to set any value for sweep preset here. The value you set in LabVIEW program for preset will be automatically transferred to MCS6 software.

APPENDIX B: DISPERSION CURVES FOR TWO DIFFERENT MASSES

```
clear all
%%input parameters%%%%%%%%%%%%%%%%%%%%%%%%%%%%%%%%%%%%%%%%%%%%%%%%%%%%%
xr=0.003;%(*distance between repeller plate and slit*)                %
vr=1530;%(*voltage on repeller plate*)                                %
L=1.346;%(*combined drift length*)                                    %
d1=0.1464;%(*distance between grid1 and grid2*)                       %
v2=802;%(*voltage on the second grid*)                                %
d2=0.0616;%(*distance between grid2 and grid3*)                       %
v3=1052;%(*voltage on the third grid*)                                %
m1=40*1.67*10.^(-27);%(*mass of the first ion*)                       %
m2=41*1.67*10.^(-27);%(*mass of the second ion*)                      %
q=1.602*10.^(-19);%(*charge*)                                         %
%%%%%%%%%%%%%%%%%%%%%%%%%%%%%%%%%%%%%%%%%%%%%%%%%%%%%%%%%%%%%%%%%%%%%%%
x=linspace(0.0014,0.002,10000);

for i=1:10000;
%%%%%%%%%%%%%%%%%%%%%%%%%%%%%%%%%%%%%%%%%%%%%%%%%%%%%%%%%%%%%%%%%%%%%%%
tlin1(i) = ((m1*xr)/(q*vr))^(1/2)*(L + x(i)*2)/((x(i)*2)^(1/2));%(*time
in linear part for the mass1*)
tlin2(i) = ((m2*xr)/(q*vr))^(1/2)*(L + x(i)*2)/((x(i)*2)^(1/2));%(*time
in linear part for the mass2*)
t12(i)=(2*d1/v2)*((m1*vr)/(q*xr))^(1/2)*((2*x(i))^(1/2)-(2*x(i)-
(2*xr*v2/vr))^(1/2));%(*time between first and second grids for the
mass1*)
t_12(i)=(2*d1/v2)*((m2*vr)/(q*xr))^(1/2)*((2*x(i))^(1/2)-(2*x(i)-
(2*xr*v2/vr))^(1/2));%(*time between first and second grids for the
mass2*)
t23(i)= (2*d2/(v3-v2))*((m1*vr)/(q*xr))^(1/2)*(((2*x(i)-
(2*xr*v2/vr))^(1/2))-(2*x(i)-2*xr*v3/vr)^(1/2));%(*time between second
and third grids for the mass1*)
t_23(i)= (2*d2/(v3-v2))*((m2*vr)/(q*xr))^(1/2)*(((2*x(i)-
(2*xr*v2/vr))^(1/2))-(2*x(i)-2*xr*v3/vr)^(1/2));%(*time between second
and third grids for the mass2*)
%%%%%%%%%%%%%%%%%%%%%%%%%%%%%%%%%%%%%%%%%%%%%%%%%%%%%%%%%%%%%%%%%%%%%%%
tof1(i)=real(tlin1(i)+t12(i)+t23(i));%(*tof for mass1*)               %
tof2(i)=real(tlin2(i)+t_12(i)+t_23(i));%(*tof for mass2*)             %
end                                                                   %

%Plotting%%%%%%%%%%%%%%%%%%%%%%%%%%%%%%%%%%%%%%%%%%%%%%%%%%%%%%%%%%%%%%
plot(x*10^3,tof1*10^6);%(*multiply by 10^3 for mm, multiply by 10^6 for
microsecond*)                                                         %
xlabel('Initial position(mm)');                                       %
xlim([1.4,2]);                                                        %
ylim([31,32.5]);                                                      %
ylabel('TOF(\mus)');                                                  %
set(findall(gcf,'type','text'),'fontSize',16,'fontWeight','normal');  %
set(gca,'FontSize',16,'linewidth',1.5,'fontweight','normal');         %
```

```
legend('CH_2CN^+','CH_3CN^+')                                                    %
hold on                                                                          %
plot(x*10^3,tof2*10^6);                                                          %
%%%%%%%%%%%%%%%%%%%%%%%%%%%%%%%%%%%%%%%%%%%%%%%%%%%%%%%%%%%%%%%%%%%%%%%%%%%%%%%
```

APPENDIX C: KINETIC ENERGY RELEASE CALCULATION

```
clear, clc
%%%%%%%%%%%%%%%%%%%%%%%%%%%%%%%%%%%%%%%%%%%%%%%%%%%%%%%%%%%%%%%%%%%%%%%%%%%%%%%%
x=0:0.0001:0.003; %%(*creates an array for the distance between       %
repeller plate and slit plate*)                                       %
V=90;%(*voltage on repeller plate*)                                   %
xr=0.003; %(*distance between repeller plate and slit*)               %
Q=1.6E-19;%(*charge*)                                                 %
M=1.67E-27;%(*mass of hydrogen*)                                      %
a=Q/M*V/xr;%(*acceleration*)                                          %
d=1.1; %(*length of the flight tube*)                                 %
v0=0;%(*initial velocity*)                                            %
%%%%%%%%%%%%%%%%%%%%%%%%%%%%%%%%%%%%%%%%%%%%%%%%%%%%%%%%%%%%%%%%%%%%%%%%%%%%%%%%
offset=-1.274*10^-6;
%%%%%%%%%%%%%%%%%%%%%%%%%%%%%%%%%%%%%%%%%%%%%%%%%%%%%%%%%%%%%%%%%%%%%%%%%%%%%%%%
t=(1/a)*(sqrt(2*a*x+v0^2)+v0)+d./sqrt(2*a*x+v0^2)+offset;%(*tof when
v0=0*)                                                                %
KE=3;%(*kinetic energy*)
v0=(3E8)*sqrt(2*KE/(938.28E6));%(*initial velocity*)
tf=(1/a)*(sqrt(2*a*x+v0.^2)+v0)+d./sqrt(2*a*x+v0.^2)+offset;%(*tof for
frontward ejected ion*)
tb=(1/a)*(sqrt(2*a*x+v0.^2)-v0)+d./sqrt(2*a*x+v0.^2)+offset;%(*tof for
backward ejected ion*)
%%%%%%%%%%%%%%%%%%%%%%%%%%%%%%%%%%%%%%%%%%%%%%%%%%%%%%%%%%%%%%%%%%%%%%%%%%%%%%%%

%%plotting%%%%%%%%%%%%%%%%%%%%%%%%%%%%%%%%%%%%%%%%%%%%%%%%%%%%%%%%%%%%%%%%%%%%%
plot(x,t*10^6,'r',x,tb*10^6,'ko',x,tf*10^6,'kx');                     %
axis([0,0.003,6,16]);                                                 %
hold on                                                               %
KE=15;                                                                %
v0=(3E8)*sqrt(2*KE/(938.28E6));                                       %
tf=(1/a)*(sqrt(2*a*x+v0.^2)+v0)+d./sqrt(2*a*x+v0.^2)+offset;          %
tb=(1/a)*(sqrt(2*a*x+v0.^2)-v0)+d./sqrt(2*a*x+v0.^2)+offset;          %
plot(x,t*10^6,'r',x,tb*10^6,'bo',x,tf*10^6,'bx');                     %
axis([0,0.003,6,16]);                                                 %
avrg_t=(tf+tb)/2;                                                     %
%%%%%%%%%%%%%%%%%%%%%%%%%%%%%%%%%%%%%%%%%%%%%%%%%%%%%%%%%%%%%%%%%%%%%%%%%%%%%%%%
```

APPENDIX D: GAUSSIAN FITTINGS

```
clear all
%% import data%%%%%%%%%%%%%%%%%%%%%%%%%%%%%%%%%%%%%%%%%%%%%%%%%%%%%%%%%%
p=importdata('Filename');                                              %
y=smooth(p.data(70000:96000),100);                                     %
t=7:0.0001:9.6;                                                        %
x=t';                                                                  %
%%%%%%%%%%%%%%%%%%%%%%%%%%%%%%%%%%%%%%%%%%%%%%%%%%%%%%%%%%%%%%%%%%%%%%%%


%%Gaussians%%%%%%%%%%%%%%%%%%%%%%%%%%%%%%%%%%%%%%%%%%%%%%%%%%%%%%%%%%%%%
L=[0 0 0 0 0 0 0 0 0];%(*Lowest limits for height position and width of
three peaks*)
U=[5 10 10 7 10 10 5 10 10];%(*Upper limits for height position and
width of three peaks*)
S=[1 7.95 .5 1 8.95 .09 1 9.25 0.09];%(*Starting points for height
position and width of three peaks*)
%%%%%%%%%%%%%%%%%%%%%%%%%%%%%%%%%%%%%%%%%%%%%%%%%%%%%%%%%%%%%%%%%%%%%%%%


%% Plotting%%%%%%%%%%%%%%%%%%%%%%%%%%%%%%%%%%%%%%%%%%%%%%%%%%%%%%%%%%%%%
f = fit(x,y,'gauss3','Lower',L,'Upper',U,'Start',S)                    %
AB=[f.b1 f.b2 f.b3];%(*creates list for height, position and width of  %
the three peaks after fitting*)                                        %
plot(f,x,y);                                                           %
%%%%%%%%%%%%%%%%%%%%%%%%%%%%%%%%%%%%%%%%%%%%%%%%%%%%%%%%%%%%%%%%%%%%%%%%
```

APPENDIX E: ATI KINETIC ENERGY CONVERSION

```
clear, clc
%%%%%%%%%%%%%%%%%%%%%%%%%%%%%%%%%%%%%%%%%%%%%%%%%%%%%%%%%%%%%%%%%%%%%%%%%%%%

Emin=0.01*1.602*(10)^(-19); %(J=kg*(m)^2/(s)^2)

Emax=10.01*1.602*(10)^(-19);
deltaE=0.01*1.602*(10)^(-19);
E=(Emin:deltaE:Emax);% (*x vector(energy)*)
d=0.39; %(*distance from the laser focus to the MCP (m)
(*play around to get exact distance by checking ati data which has peak
separation by 1.55 eV photon energy*)
m=9.11*(10)^(-31);%(*mass of electron*)
%%%%%%%%%%%%%%%%%%%%%%%%%%%%%%%%%%%%%%%%%%%%%%%%%%%%%%%%%%%%%%%%%%%%%%%%%%%%

%%IMPORTDATA%%%%%%%%%%%%%%%%%%%%%%%%%%%%%%%%%%%%%%%%%%%%%%%%%%%%%%%%%%%%%%%
ati=importdata('Filename');
data=ati.data;
T=(1:1:length(data))*10^-10;%(*creates numbers from zero to number of
data and converts it to second*)
%%%%%%%%%%%%%%%%%%%%%%%%%%%%%%%%%%%%%%%%%%%%%%%%%%%%%%%%%%%%%%%%%%%%%%%%%%%%

%%Kinetic energy conversion%%%%%%%%%%%%%%%%%%%%%%%%%%%%%%%%%%%%%%%%%%%%%%%%
j=(Emax-Emin)/deltaE+1;
for k=1:j-1;
t(k+1)=d*((m./(2*E(k+1))))^(1/2);
F=find(T>t(k+1)&T<t(k));
S(k)=sum(data(min(F):max(F)));
end
t(1:j-1);
F;
X=S(1:j-1); X2=X;
Y=E(1:j-1)/(1.602*10^(-19)); Y=Y';
X=X/sum(X); X=X';
%%%%%%%%%%%%%%%%%%%%%%%%%%%%%%%%%%%%%%%%%%%%%%%%%%%%%%%%%%%%%%%%%%%%%%%%%%%%

%%Plotting%%%%%%%%%%%%%%%%%%%%%%%%%%%%%%%%%%%%%%%%%%%%%%%%%%%%%%%%%%%%%%%%
semilogy((Y-0.61),smooth(X2,5),'LineWidth',2); title(['60 mW']);
xlabel('energy (eV)'); ylabel('count (arb. unit)');
set(findall(gcf,'type','text'),'fontSize',20,'fontWeight','normal');
set(gca,'color','white','FontSize',20,'linewidth',2,'fontweight','norma
l');
xlim([0,7]);
%%%%%%%%%%%%%%%%%%%%%%%%%%%%%%%%%%%%%%%%%%%%%%%%%%%%%%%%%%%%%%%%%%%%%%%%%%%%
```